Bachelor's thesis

Electronics & Communications Engineering

2019

Mohamed Räsänen

DESIGN AND ANALYSIS OF AN ANALOG BEAMFORMING TRANSMIT SYSTEM FOR 5G MIDBAND FREQUENCIES

TURKU AMK

TURKU UNIVERSITY OF APPLIED SCIENCES

Mohamed Räsänen

DESIGN AND ANALYSIS OF AN ANALOG BEAMFORMING TRANSMIT SYSTEM FOR 5G MIDBAND FREQUENCIES

Due to the increased users of wireless communications and stringent data applications, the demand for increased bandwidth is yet unrelieved. While 4G long-term evolution (LTE) is reaching the limits of time and frequency resource utilization, various beamforming techniques have been analyzed for the upcoming 5G technology. Beamforming has been the most promising space division multiple access (SDMA) technique for increasing capacity. In beamforming a phased array antenna is used, which includes multiple radiating elements. By providing the calculated phase and amplitude excitations at each elements, the beams and nulls can be steered to the desired directions, thus allowing the multiple input multiple output (MIMO) technology to be implemented.

The objective of this thesis was to design, construct and analyze a beamforming transmit system. Thesis consists of a brief overview of existing beamforming techniques and a design process for an eight element analog beamforming transmit system for 5G mid band (3.4GHz – 3.8GHz) frequencies. Design was conducted with NI AWR Design Environment and Mentor PADS- software. The pcb assembly was conducted by hand and by using a BGA rework station. Lastly RF measurements were performed for the system. Receive beamforming was not assigned for the system.

The beamformer allows signal transmission at 5G midband frequencies (3.4GHz – 3.8GHz), which are allocated for most of Europe. Beamsteering was conducted with analog beamforming principles by using phase weightings.

KEYWORDS:

Beamforming, phased array antenna, 5G, SDMA, RF Design, MMIMO

Mohamed Räsänen

ANALOGISEN KEILANMUODOSTUSLÄHETINJÄRJESTELMÄN SUUNNITTELU JA ANALYYSI 5G-KESKIKAISTATAAJUUKSILLE

Kasvaneen langattoman tietoliikenteen käyttäjämäärien sekä nykyisten tiedonsiirtosovellusten vaativuuden vuoksi on tarve suuremmalle kapasiteetille riittämätön. Sillä aikaa kun 4G long-term evolution (LTE) on saavuttamassa rajansa taajuus- sekä aikatason resurssien käytössä, on erilaisia keilanmuodostustekniikoita analysoitu tulevalle 5G-teknologialle. Keilanmuodostus on ollut lupaavin tilanjakokanavointitekniikka kapasiteetin kasvattamiselle.

Keilanmuodostuksessa käytetään vaiheohjattua antenniryhmää, jossa on usea säteilevä elementti. Tuottamalla lasketut vaihe- sekä amplitudiarvot voidaan pääkeiloja ja nollakohtia ohjata eri suuntiin. Näin saadaan etuja kapasiteetin kasvulle sekä mahdollistetaan multiple input multiple output (MIMO) -teknologia.

Opinnäytetyössä tehtiin yleiskatsaus olemassaolevista keilanmuodostusmenetelmistä sekä suunniteltiin kahdeksanelementtinen analoginen keilanmuodostuslähetinjärjestelmä 5G-keskikaistataajuuksille (3,4GHz – 3,8GHz). Suunnittelussa käytettiin NI AWR Design environment ja Mentor Graphics PADS -ohjelmistoja. Piirilevyn kokoonpano toteutettiin käsin, minkä jälkeen suoritettiin mittaukset. Keilanmuodostuksen vastaanotinosiota ei määrätty järjestelmälle.

Järjestelmä mahdollistaa signaalin lähetystä analogisella keilanmuodostustekniikalla 5G-keskikaistataajuuksilla (3,4GHz – 3,8GHz), jotka on sijoitettu isolle osaa Eurooppaa. Keilanohjaus toteutettiin vaiheenpainotuksilla.

ASIASANAT:

Keilanmuodostus, vaiheohjattu antenni, 5G, tilanjakokanavointi, RF- suunnittelu

CONTENTS

LIST OF ABBREVIATIONS AND SYMBOLS

ABF	Analog beamforming
BGA	Ball grid array
CSI	Channel state information
D2D	Device to device
dB	Decibel
DBF	Digital beamforming
DOA	Direction of arrival
GHz	Gigahertz
GUI	Graphical user interface
HBF	Hybrid beamforming
IoT	Internet of things
IoV	Internet of vehicles
I/O	Input/output
LPF	Low pass filter
LTE	Long term evolution
M2M	Machine to machine
MCU	Microcontroller unit
MIMO	Multiple input multiple output
MMIMO	Massive multiple input multiple output
MmWave	Millimeter wave
nH	nanoHenry
OABF	On-off analog beamforming
OCSR	Open circuit stub resonator
PCB	Printed circuit board
pF	picoFarad
PS	Phase shifter

RF	Radio frequency
SDMA	Spatial division multiple access
SILPF	Stepped impedance low pass filter
$\lvert \cdot \rvert$	Absolute value
$[\, : \, : \,]$	Matrix
$*$	Complex conjugate
π	Ratio of a circle's circumference to its diameter
$e^{[\cdot]}$	Exponential function
Σ	Summation operator
sin	Sine function
sinh	Hyperbolic sine function
coth	Hyperbolic cotangent function
$\log_{10}$	Base 10 logarithm
$\in$	Set membership operator
AF	Array factor
a_n	Amplitude weighting for an array
A_{tot}	Total attenuation
c	Speed of light
C	Capacitance
C_n	Chebyshev polynomial
d	Inter-element distance
f_r	Resonance frequency
g_k	g- parameters for Chebyshev filter
h	Height between the transmission line and bottom conductor
k	Wavenumber
K	Power ratio coefficient
l	Length of a transmission line
L	Inductance
L_r	Passband ripple factor

M	Number of radiating elements
P	Power
R	Resistance
R_{DSon}	Drain-source on resistance
t	time, thickness of a transmission line
w	Width of a transmission line
w^*_m	Complex weight for mth antenna element
v_0	Speed of light
$x(t)$	Output of antenna element
$y(t)$	Output of beamformer
Z	Impedance
Δ	Difference
$\Delta\varphi$	Phase difference
$\mathcal{E}_{eff}$	Effective dielectric constant
$\mathcal{E}_r$	Relative dielectric constant
λ	Wavelength
λ_g	Guided wavelength
Ω	SI- unit for resistance
Ωc	Cut-off frequency factor
ω_c	Cut-off frequency
Φ	Azimuth angle
θ	Zenith angle

1 INTRODUCTION

There has been a global rise in mobile wireless communications access for the global population. The improvement of mobile broadband quality and reach has generated an insatiable demand for mobile communications and IoT applications. According to a forecast update (2017-2022) conducted by Cisco VNI Mobile Forecast [1], mobile traffic will be on the threshold of reaching an annual run rate of a zettabyte by the end of the forecast period. Mobile traffic will represent nearly 20% of global IP traffic and will reach 930 exabytes annually by 2022, which is nearly 113 times more than all global traffic generated in 2012. It is estimated that by 2022 there will be an increase from 5 billion to 5.7 billion mobile users, which represents 71% of the global population. Mobile networks will support more than 8 billion personal mobile devices and 4 billion IoT connections by 2022. The forecast update anticipates that the average global mobile network speeds will increase more than 3- fold from 8.7Mbps in 2017 to 28.5Mbps by 2022. Average mobile speeds vary by geographic locations as 5G will be adopted in various regions. 5G will represent 3.4% of connections but 11.8% of total traffic by 2022 and it will generate 2.6 times more traffic than the average 4G connection. Figure 1 illustrates the global mobile data drivers [1, 2].
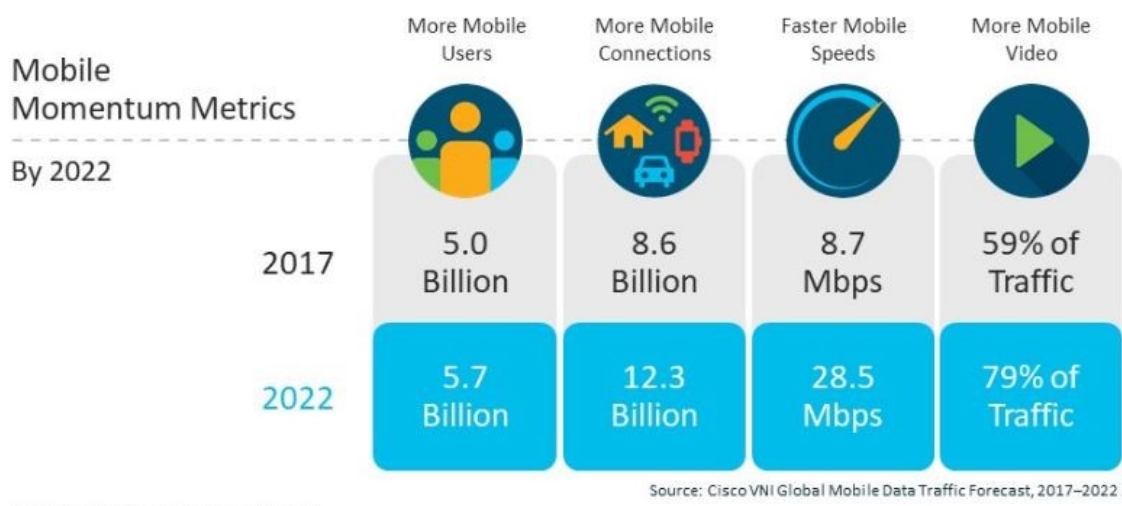
Figure 1: Global Mobile Data Drivers according to reference [2].

One of the key technologies to allow the vast growth of global mobile data usage lies within beamforming.

Thesis begins with a review of the applications of beamforming in wireless communications and a brief overview of existing beamforming methods and techniques. The main objective of this thesis is to design and analyze an 8-element analog beamforming transmit system for the 5G midband frequencies (3.4-3.8GHz) that are allocated for most of Europe [10]. The beamformer enables a company to use the beamformer for transmitting the previously mentioned frequencies by using analog beamforming principles. The software architecture and GUI (Graphical user interface) has been designed for this system in another thesis.

The thesis is structured as follows: Chapter 1 introduces the background and the objectives of the thesis. Chapter 2 includes the applications of beamforming, linear antenna array theory and an overview of existing beamforming methods. The design process of the beamformer is presented in Chapter 3. Chapter 4 shows the measurement results of the beamformer. Finally, Chapter 5 contains the conclusions.

2 BEAMFORMING

Beamforming is a spatial filtering technique which has been widely used in radar, sonar, signal processing, biomedical and communications. In signal processing, beamforming is used for directional signal transmission and reception. By combining radiating elements in a specific way in a phased array antenna, the signals will achieve constructive interference at certain angles while others achieve destructive interference. Further theory on linear antenna arrays is provided in Section 2.1. The summation of these interferences will allow the signals to be transmitted to desired directions or received from the directions of interest [11, 12, 14-16, 19, 21, 22, 26]. Applications of beamforming is depicted in Figure 2, which is obtained from reference [12].
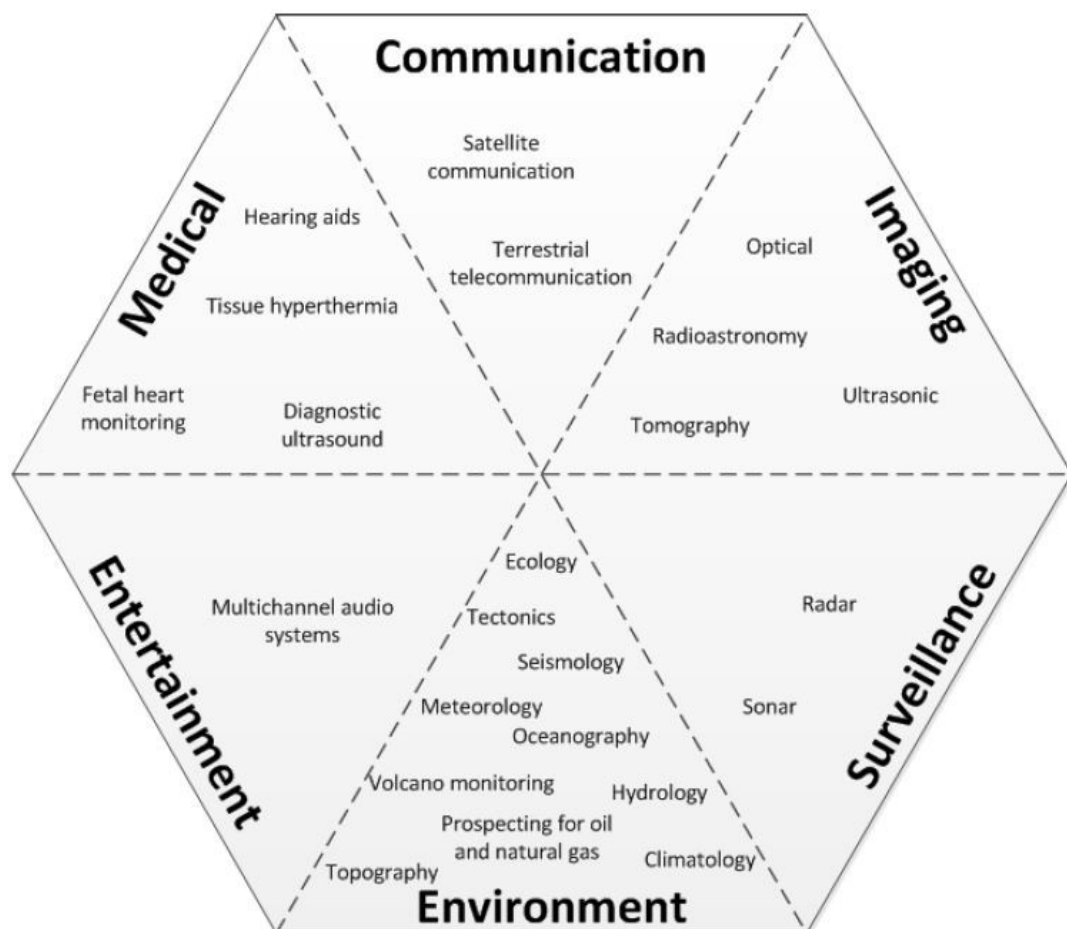

Figure 2: Applications of beamforming [12].

The 4G mobile communication system is challenged to meet the upcoming demands on the spectrum and power efficiency. MMIMO (massive multiple input multiple output) is a technology that uses beamforming and is currently being researched to overcome the challenges regarding the future of wireless mobile communications. As an extension of traditional MIMO technology, MMIMO can vastly improve throughput rate and energy efficiency [3, 4].

MMIMO is a SDMA -based multiplexing technique. SDMA has its origins in satellite communications. SDMA technique allows the simultaneous use of a radio channel by multiple users within the same cell by taking into account their spatial position, thus a smart antenna is used to dynamically optimize the transmission and reception of the radiation patterns in response to the surrounding environment. A factor that limits the capacity increase of a communication system is the co-channel interference, which is a product of the reuse of the available channels within the system. With the use of SDMA, the co-channel interference is reduced significantly by using beamforming [5, 6]. An illustration of SDMA technique is depicted in Figure 3.
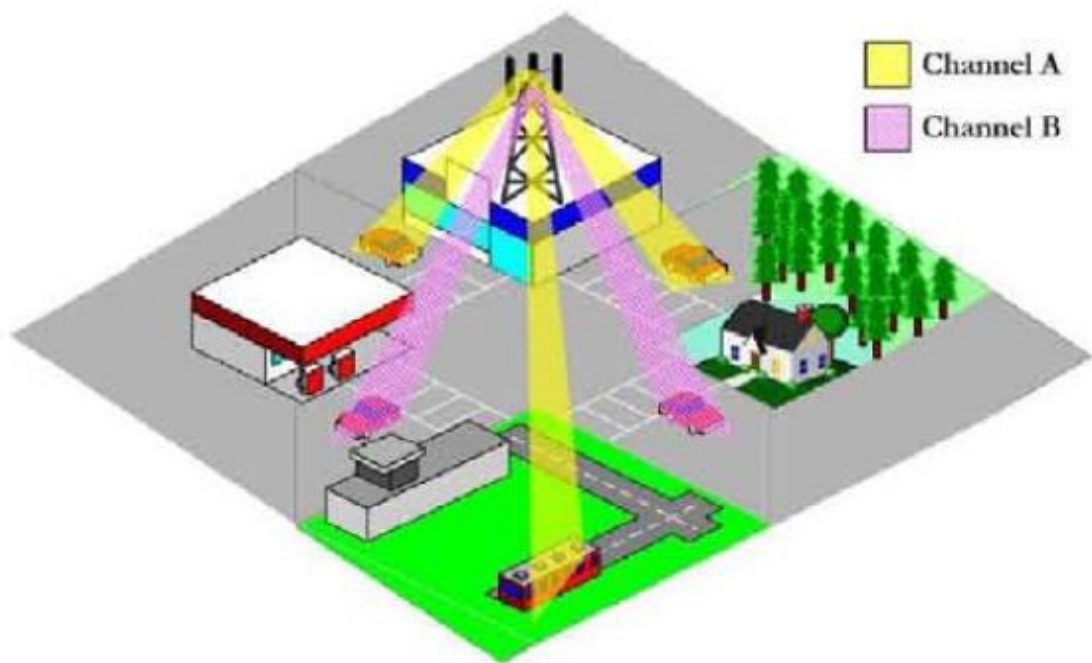

Figure 3: Illustration of the SDMA technique according to [5].

According to references [7, 8], MMIMO has been demonstrated to achieve an order-of-magnitude higher spectral efficiency with practical CSI. 3GPP is steadily increasing the

maximum number of antennas in LTE and since 64 antennas are supported in release 15, MMIMO has become an integral part of 5G. Another key approach to increase the capacity of future wireless networks is the operation in mmWave bands, as the frequency spectrum above 30GHz can be used as a complement to the current sub-6GHz bands.

MmWave massive MIMO will be used in a broad range of technologies including M2M (machine to machine), IoV (internet of vehicles), D2D (device to device), backhaul, access, small cells, vertical virtual sectorization, etc. MMIMO is depicted in Figure 4.
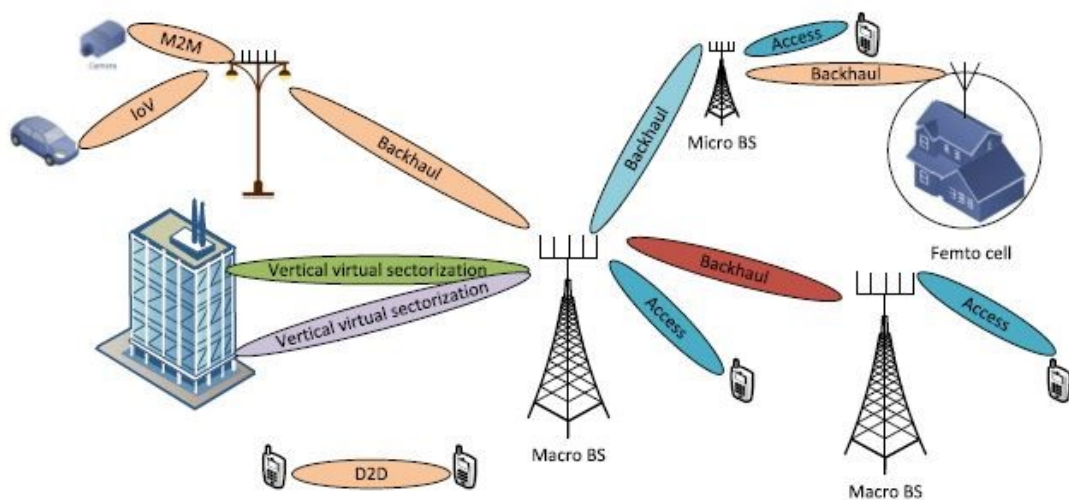

Figure 4: MmWave massive MIMO beamforming applications in 5G wireless networks according to reference [9].

The 5G spectrum is divided within three key frequency ranges to support all user causes and deliver widespread coverage. They are: Sub-1GHz, 1-6GHz and above 6GHz [10].

The sub-1GHz spectrum is used to extend high speed 5G mobile broadband coverage across suburban, urban and rural areas and to support IoT devices. The European Commission supports the use of 700MHz band for 5G services and in the United States, T-Mobile has announced its plans to use 600MHz for 5G [10].

1-6GHz offers a mixture of coverage and capacity for 5G. According to [10], "It is vital that regulators assign as much contiguous spectrum as possible in the 3.3-3.8 GHz and also consider the 4.5-5GHz and 3.8-4.2GHz".

A spectrum above 6GHz is needed for 5G services such as ultra high-speed mobile broadband. These bands are essential for delivering the fastest dataspeeds in 5G.

One of the key components in a beamformer is the antenna array. Figure 5 illustrates a simple beamforming structure based on a linear array, where M elements sample the wave field spatially and the output of the beamformer $y(t)$ at time t is given by the linear combination of these spatial samples $x_m(t)$, m = 0, 1, … M-1, as equation (1) [11] depicts.

$$y(t) = \sum_{m=0}^{M-1} w_m^* x_m(t) \qquad (1)$$

Where $x_m(t)$ is the output of the antenna element, w_m^* is the complex weight for the antenna element and * denotes the complex conjugate. The beamformer associated with this structure is only useful for sinusoidal or narrowband signals. Hence it is termed a narrowband beamformer [11].

The time domain response of the array can be analyzed to an impinging complex plane wave $e^{j\omega t}$ with an angular frequency ω and DOA (direction of arrival) angle θ, where $\theta \in [-\pi/2 \; \pi/2]$ is measured with respect to the broadside of the linear array, as shown in Figure 5. It is assumed that the phase of the signal is zero at the first element. The signal received by the first element is then $x_0(t) = e^{j\omega t}$ and by the mth element is $x_0(t) = e^{j\omega(t-\tau m)}$, m = 1, 2, … M-1, where τm is the propagation delay for the signal from sensor 0 to sensor m and is a function of θ. The beamformer output is then [11]:

$$y(t) = e^{-j\omega t} \sum_{m=0}^{M-1} e^{-j\omega \tau_m} w_m^* \qquad (2)$$
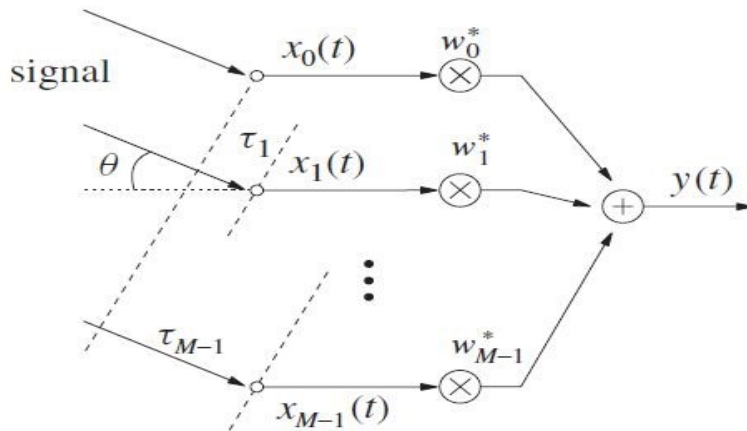
The operation principle is depicted in Figure 5.

Figure 5: A general structure for narrowband beamforming with a linear array [11].

2.1 Linear array antenna theory

A linear array antenna is a one dimensional array composed of radiating elements with regular distances between each element and its maximum coverage in the azimuthal plane is usually ±60° [11- 15]. A linear antenna array is assumed that contains an n number of equally spaced isotropic radiating elements. Elements can be placed along the x-axis of a spherical coordinate system as shown in Figure 6 [13].
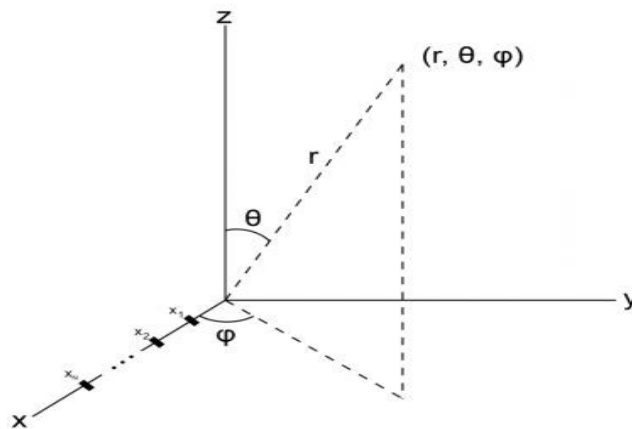

Figure 6: Linear antenna array [13].

The radiation pattern F_{array} of a linear antenna array is approximated by multiplying the array factor AF_{array} with the element radiation pattern $F_{element}$ that is considered equal for all elements assuming an array large enough.[13, 14]. F_{array} can be calculated by:

$$F_{array}(\theta, \phi) = F_{element}(\theta, \phi) AF_{array}(\theta, \phi) \tag{3}$$

And the array factor AF_{array} by:

$$AF_{array}(\theta, \phi) = \sum_{n=1}^{N} a_n e^{jnkd \, sin\theta sin\phi} e^{j\Delta\varphi} \tag{4}$$

Where a_n is the amplitude weight factor per element, k is the wavenumber $2\pi/\lambda$, d is the inter-element distance and $\Delta\varphi$ is the phase difference between the signals and is depicted in Section 2.2.1.

Equation (4) can be simplified by adding the far-zone phase difference ψ between adjacent elements [13, 14]:

$$\psi = kd \, \sin\theta \sin\phi + \Delta\varphi \tag{5}$$

Substituting (5) in equation (4) results in [13]:

$$AF_{array}(\theta, \phi) = \sum_{n=1}^{N} a_n \, e^{jn\psi} \tag{6}$$

The series in (6) can be normalized to the normalized array factor by [13, 14]:

$$\left| AF_{array}(\psi) \right| = \frac{1}{N} \left| \frac{\sin(N\psi/2)}{\sin(\psi/2)} \right| \tag{7}$$

2.1.1 Radiation pattern altering factors

The number of elements and their equidistant spacing have a significant influence on the characteristics of a linear antenna array as implied by equations (4) – (7). The effects of modifying these two parameters will be explained in this section and visual representation is illustrated in Figure 7 [13].

2.1.2 Number of radiating elements

The number of radiating elements and their equidistant spacing defines the characteristics of the linear antenna array. The main lobe width decreases as a function of element count, thus the directivity of the linear array increases. The number of sidelobes and nulls with lower levels also increase as elements are added [11- 15]. The effects of the number of radiating elements are illustrated in Figure 7 [13].

2.1.3 Element spacing

The directivity of a linear array can also be improved by increasing the distance between elements, which yields a narrower main lobe. The number of side lobes will increase, although without reduced power levels. The extra main lobes created by large element spacing are called grating lobes and they are periodically located at intervals inversely proportional to the element spacing. In reception the grating lobes cause directional ambiguity due to the arrival of signals from the direction of the main beam or the grating lobe, thus resulting in the same response. During transmission the transmitted power experiences parasitic loss towards grating lobes, since the task is to project the energy towards the receiver. The power transmitted towards grating lobes can also cause interference to other users. However grating lobes can be used for benefit in transmission diversity for example [11- 15].

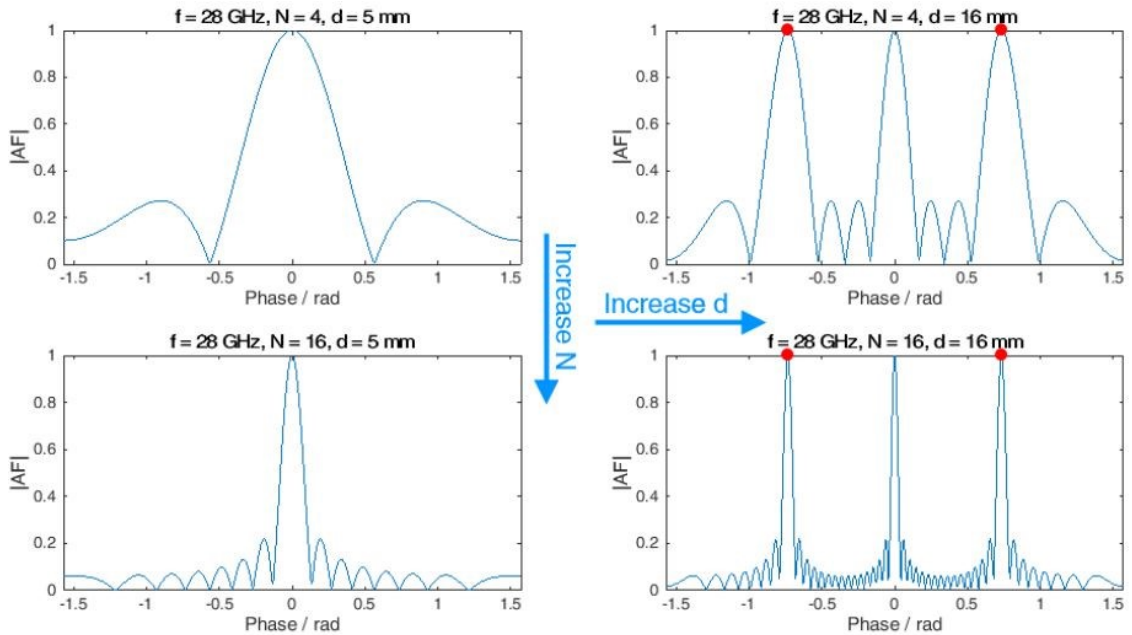The effect of element spacing can be observed in Figure 7 [13].

Figure 7: Normalized array factor for multiple configurations, obtained from [13].

The red dots in Figure 7 highlight the grating lobe effect for the antenna with a spacing of 1.5λ. The diagrams on the left describe the normalized array factor $|AFarray(\psi)|$ for an antenna array with an equidistant spacing of 5mm between elements, which is slightly lower than 0.5λ at 28GHz. The normalized array factor of an antenna with a spacing of 16mm, which corresponds roughly to 1.5λ, is displayed on the right side. Diagrams on the upper half were calculated for an array of four elements, while the array factors displayed in the lower half are from a 16 element array [13].

The grating lobes start to equal the main lobe level after an element spacing of λ. In order to prevent grating lobes from appearing in the visible region, which is defined as the range [-90° 90°], the following condition must be maintained [13, 14, 15] :

$$d < \frac{\lambda}{2} \qquad (8)$$

Additional option for eliminating grating lobes is to restrict the scan angle by using the grating lobe equation, where $|\theta_0|$ is the maximum scan range [13, 14, 15]:

$$\sin|\theta_0| \le \frac{\lambda}{d} - 1 \qquad (9)$$

2.2 Beamforming methods

Numerous beamforming methods have been developed and studied [16 - 18, 21, 25, 26]. Each method has its advantages and disadvantages. In order to determine which method is to be used in a particular situation, one must be aware of the benefits and downsides of each architecture, which are discussed in the following sections.

2.2.1 Analog beamforming

Analog beamforming is a process, where the signal's amplitude and/or phase is manipulated in the analog domain at the RF frequencies or intermediate frequency [13]. Figure 8 illustrates a basic implementation of an analog beamforming transmitter architecture. Analog beamforming is generally restricted to one RF chain.
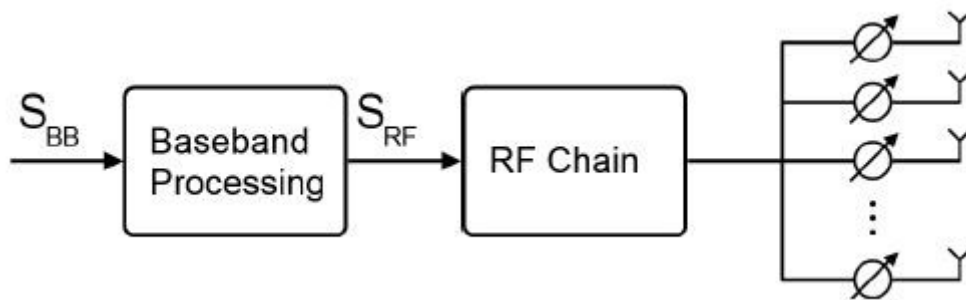

Figure 8: Analog beamforming architecture [13].

The first practical beamforming antennas date back to 1961, where beam steering was conducted by implementing a selective RF switch and fixed phase shifters. The basics of this method are still used to date, however with advanced and improved precoding algorithms. These enhancements enable individual control of the phase of each element. Analog beamforming is used today in high-end millimeter-wave systems as diverse as radar and short-range communication systems such as IEEE 802.11ad. These architectures have reduced complexity and are not as expensive as the other approaches described in Sections 2.4.2 and 2.4.3. However, the challenge to analog beamforming architecture is the complexity to produce multi-stream transmission [13, 16].

To calculate the phase weightings, a uniformly spaced linear array with element spacing d is assumed. Considering the receive scenario shown in Figure 9, the antenna array must be in the far field of the incoming signal in order to receive an approximately planar wavefront. If the signal arrives at an angle θ off the antenna boresight, the wave must travel an additional distance of $d \sin \theta$ to arrive at each successive element as shown in Figure 9. This can be viewed as an element specific delay which can be converted to a frequency dependent phase shift of the signal [13].

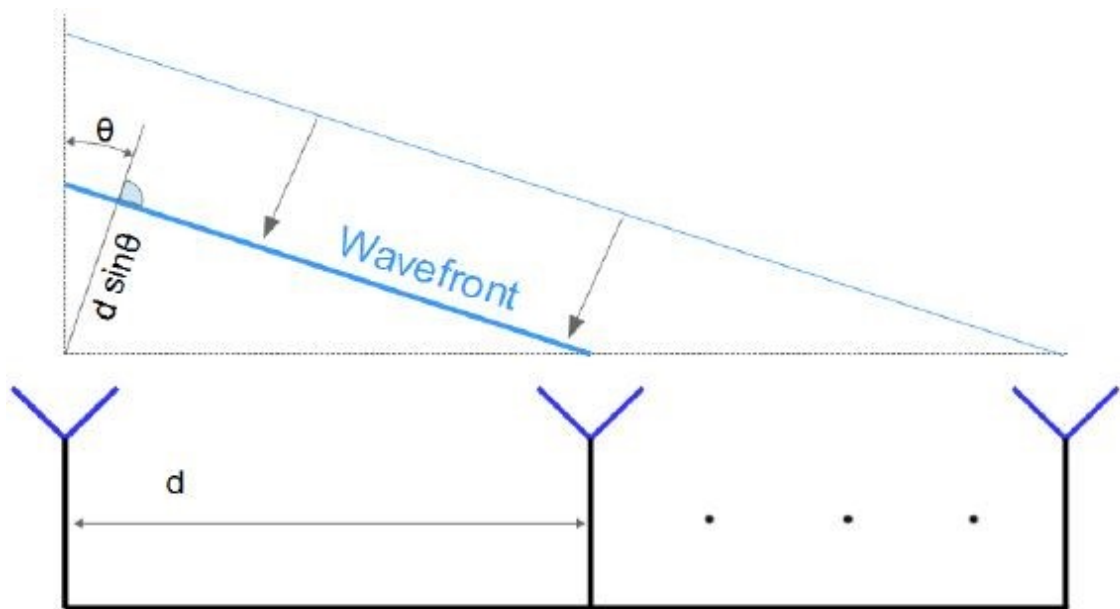$$\Delta\varphi = \frac{2\pi}{\lambda} d \sin \theta \qquad (10)$$

Figure 9: Additional travel distance when signal arrives off boresight according to [13].

The frequency dependency manifests itself as an effect called beam squint. The main lobe of the antenna array at a defined frequency can be steered to a certain angle using phase offsets calculated with equation (10). If the antenna elements are fed with a signal of a different frequency, the main lobe will be offsetted by a specific angle. Since the phase relations were calculated with a certain carrier frequency, the angle of the main lobe shifts according to the present frequency. Radar applications with large bandwidths for example suffer inaccuracies due to this phenomenon [13].

Equation (10) can be rendered frequency independent by using time delays instead of frequency offsets as shown in (11) [13].

$$\Delta t = \frac{d \sin \theta}{c} \tag{11}$$

The setup is fitted with delay lines instead of phase shifters. The corresponding receiver setup is shown in Figure 10 [13]. The delay lines t_0 to t_2 compensate for the time delay Δt, which is an effect of the angle of the incident wave. Thus, the received signals are theoretically perfectly aligned and will add constructively when summed together [13].
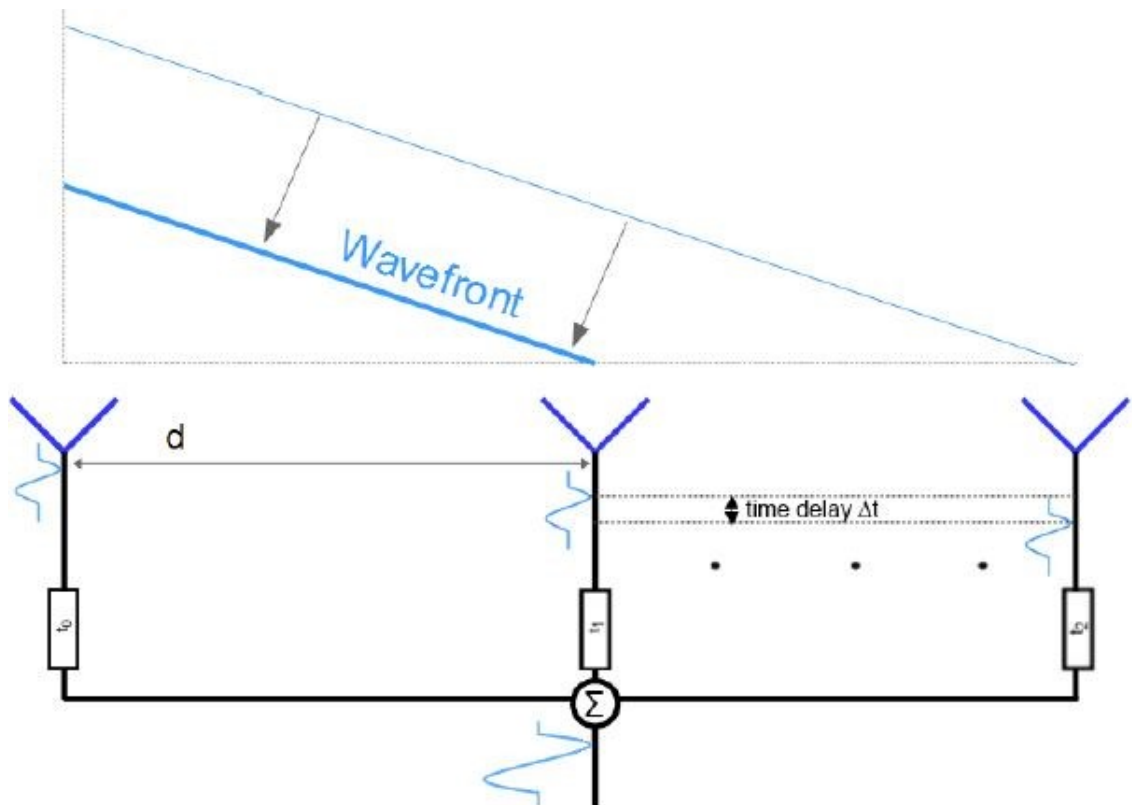

Figure 10: True time delay beamsteering [13].

The performance of the analog architecture can be further improved by varying the amplitudes of the signals incident to the radiating elements[13]. Equations (10) and (11) can also be used for transmit beamforming [19].

A recent subject of study regarding to analog beamforming is on-off analog beamforming (OABF). OABF implements RF switches before the transmit antennas to form a beam according to the CSI at transmitters. This translates to even reduced hardware and algorithm complexities, where phase shifters are not needed [17]. According to the previously referenced article, OABF is believed to make MMIMO much easier to implement in real systems. Figure 11 [17] illustrates the OABF transmitter architecture.
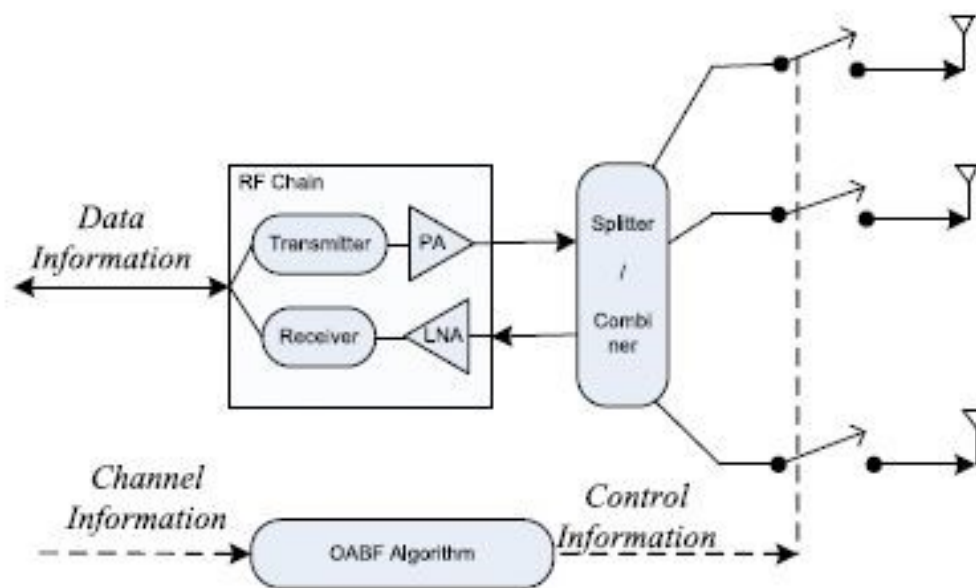

Figure 11: OABF Transmitter architecture [17].

The aim of OABF is to form beams without any phase and amplitude pre-processing neither in the analog domain nor in the digital domain [17].

2.2.2 Digital beamforming

Early ideas that form the foundations of DBF (digital beamforming) were first developed in the fields of sonar and radar systems. A major advantage provided by DBF is that once the RF information is captured in the form of a digital stream, digital signal processing techniques and algorithms can be applied to the spatial domain data. DBF is based on the conversion of the RF signal at each radiating elements into two streams of binary baseband signals representing I and Q channels, which represent the amplitudes and phases of signals received at each element of the array. The beam decided by the array factor is formed in the digital domain [20, 21].

DBF in theory supports as many RF chains as there are radiating elements. Each antenna requires its own RF chain. If precoding is applied in the digital baseband, improvements in higher flexibility regarding the transmission and reception is achieved. DBF enables advanced techniques such as multi-beam MIMO. This architecture has the highest theoretical performance possible compared to other beamforming architectures [13, 18, 20-23]. Figure 12 [13] illustrates the general DBF transmitter architecture.
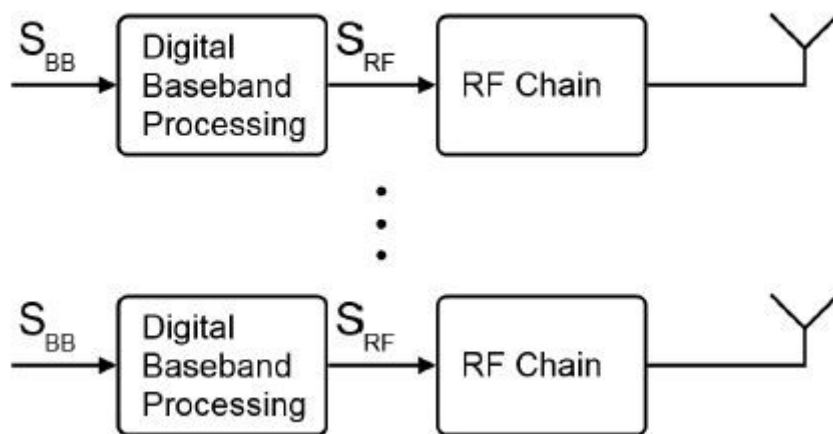

Figure 12: Digital beamforming architecture [13].

Digital control of the RF chain allows optimization of the signal's phases over a wide band. However DBF is very complex with regarding hardware and is very costly compared to other architectures. The power consumption of DBF and complicated integration to mobile devices implies that this architecture is better suited for use in base stations, since performance plays a greater role than mobility in this situation [13, 20].

2.2.3 Hybrid beamforming

A significant cost reduction can be achieved by reducing the number of complete RF chains, thus leading to a lower overall power consumption. Since the number of converters is significantly lower than the number of antennas, there is less freedom for digital baseband processing. This translates to reduced number of simultaneously supported streams when compared to DBF. The hybrid beamforming architectures are broadly divided into fully connected, in which each RF chain is connected to all antennas, and sub-connected, in which each RF chain is connected to a set of antenna elements. The objective of all hybrid beamforming architectures is to reduce complexity with regarding hardware and signal processing while providing performance comparable to DBF. HBF (Hybrid beamforming) is able to achieve a large antenna array gain and perform digital baseband processing. There is a growing interest in whether HBF is a suitable architecture which can exploit large mmWave antenna array with reduced architecture. Hybrid beamforming is able to obtain the array gain of an analog beamformer and the speed and multibeam capability of a digital beamformer [13, 16, 18, 24, 25]. Figure 13 depicts the two hybrid beamforming architectures.
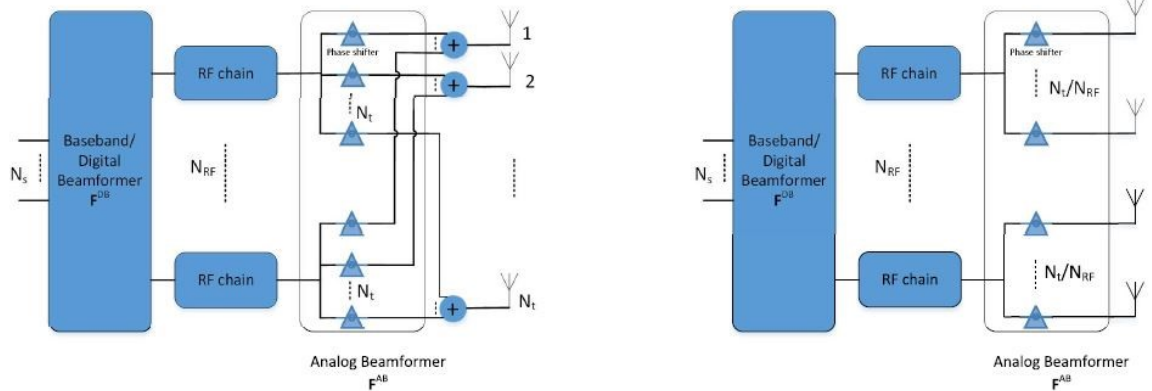
(a) Fully connected HBF   (b) Sub-connected HBF

Figure 13: Major types of HBF [18].

3 DESIGN OF AN ANALOG BEAMFORMING TRANSMIT SYSTEM

The design process for the 8-element analog beamforming transmit system is described in this chapter. System operates by controlling 6-bit MMIC phase shifters with 8-bit shift registers and a MCU. Microstrip components were designed and simulated with NI AWR Design Environment and then ported to Mentor Graphics PADS. After PCB design the board was then ordered and components were soldered by hand and by using a BGA rework station. After the PCB was constructed along with the mechanical casing, the system was tested for its performance.

3.1 Block diagram

First a block diagram was designed as depicted in Figure 14. The signal is first fed through a driver amplifier before it is equally divided into eight outputs with a Wilkinson power divider. Signals are then fed into the phase shifters and passed through second stage amplification and a LPF. Phase shifting is conducted through digital logic control.
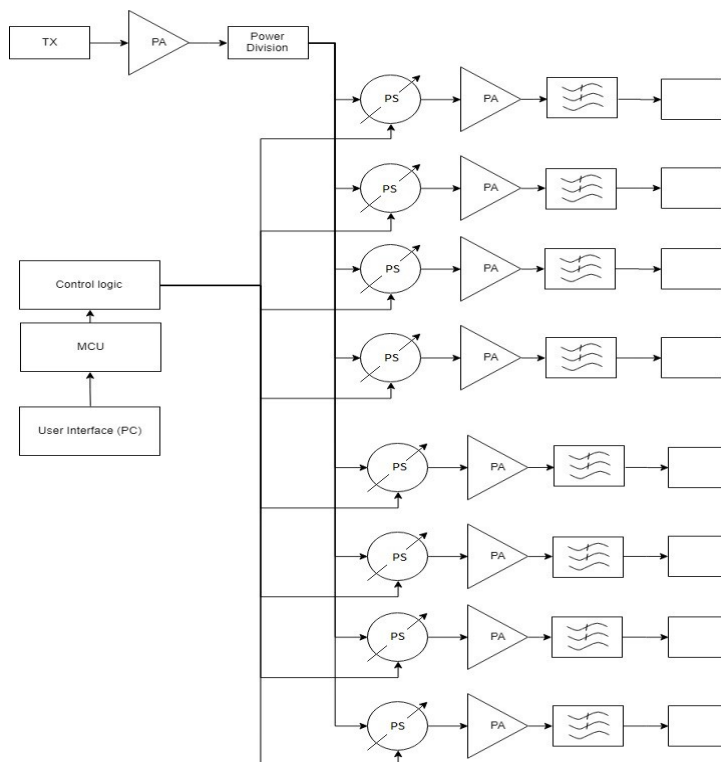
Figure 14: System block diagram.

3.2 Digital Interface

The digital interface was implemented by controlling 8-bit serial-in, parallel-out shift registers and an STM32F091RC MCU. With this design, it is possible to control a large number of phase shifters with only three I/O pins from a MCU. Digital interface is illustrated in Figure 15.
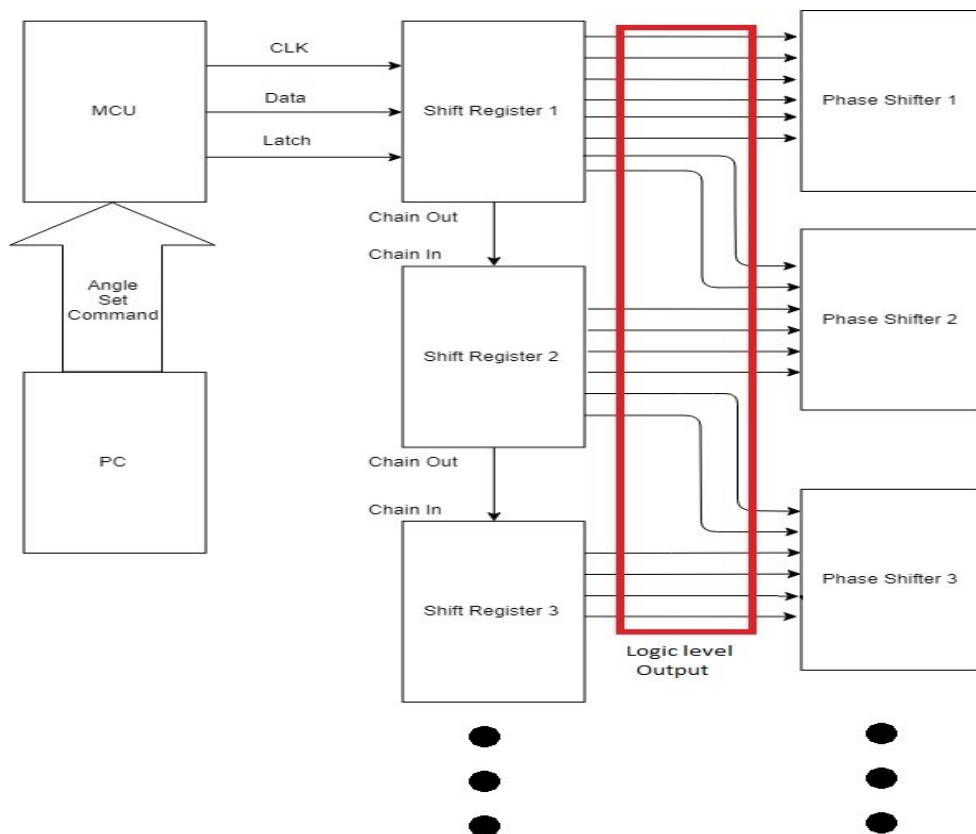
Figure 15: Digital interface.

The shift register accepts data from the serial input on each rising edge of the shift register clock. Data from the input register is outputted to the parallel register with a rising pulse on the storage register clock (Latch). The chosen shift register was 74HCT595, a high speed CMOS device that has a low V_{ih} (High- level input voltage) of 2V. This ensures that the device can be controlled with 3.3V logic signals, while outputting 5V logic levels for the phase shifters [26].

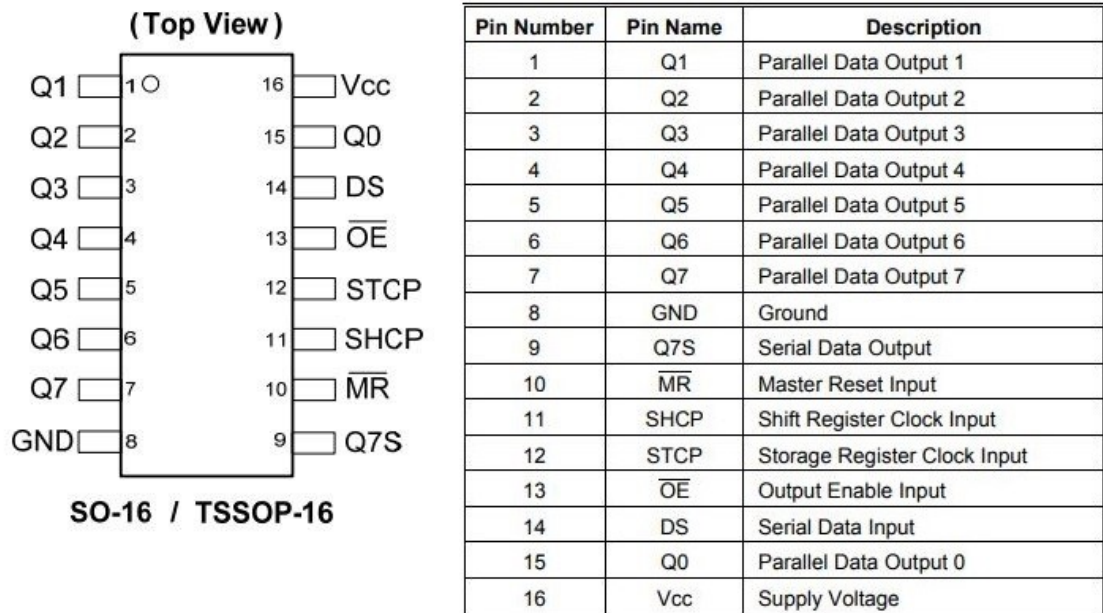Figure 16 shows the pin mapping and descriptions for the shift register.

Pin Number	Pin Name	Description
1	Q1	Parallel Data Output 1
2	Q2	Parallel Data Output 2
3	Q3	Parallel Data Output 3
4	Q4	Parallel Data Output 4
5	Q5	Parallel Data Output 5
6	Q6	Parallel Data Output 6
7	Q7	Parallel Data Output 7
8	GND	Ground
9	Q7S	Serial Data Output
10	$\overline{MR}$	Master Reset Input
11	SHCP	Shift Register Clock Input
12	STCP	Storage Register Clock Input
13	$\overline{OE}$	Output Enable Input
14	DS	Serial Data Input
15	Q0	Parallel Data Output 0
16	Vcc	Supply Voltage

Figure 16: Pin layout and descriptions of the 74HCT595 shift register [26].

The logic diagram is presented in Figure 17:

Control				Input	Output		Function
SHCP	STCP	$\overline{OE}$	$\overline{MR}$	DS	Q7S	Qn	
X	X	L	L	–	L	NC	Low-level asserted on MR clears shift register Storage register is unchanged
X	↑	L	L	–	L	L	Empty shift register transferred to storage register
X	X	H	L	–	L	Z	Shift register remains clear; All Q ouputs in Z state
↑	X	L	H	–	Q6S	NC	HIGH is shifted into first stage of Shift Register Contents of each register shifted to next register The content of Q6S has been shifted to Q7S and now appears on device pin Q7S
X	↑	L	H	–	NC	QnS	Contents of shift register copied to storage register With output now in active state, the storage resister contents appear on Q outputs
↑	↑	L	H	–	Q6S	QnS	Contents of shift register copied to output register then shift register shifted.

H=HIGH voltage state
L=LOW voltage state
↑=LOW to HIGH transition
X= don't care – high or low (not floating)
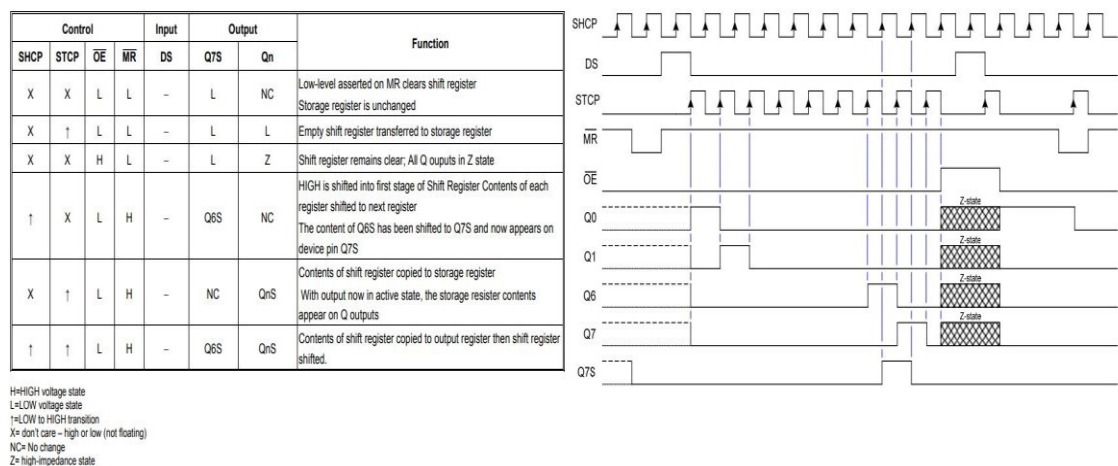NC= No change
Z= high-impedance state

Figure 17: Functional and timing diagram of the 74HCT595 shift register [26].

V_{ih} voltage conditions of the shift register are presented in Figure 18.

Symbol	Parameter	Test Conditions	V_{CC}	$T_A = +25°C°C$			$T_A = -40°C°C$ to $+85°C°C$		$T_A = -40°C°C$ to $+125°C°C$		Unit
				Min	Typ	Max	Min	Max	Min	Max	
V_{IH}	High-Level Input Voltage	–	4.5V to 5.5V	2.0	–	–	2.0	–	2.0	–	V

Figure 18: Shift register *Vih* [26].

Figure 19 depicts the PS pin mapping and truth table.

Truth Table (0 : 0V , 1 : +5V)

Phase	P1	P2	P3	P4	P5	P6
REF	0	0	0	0	0	0
-5.625°	1	0	0	0	0	0
-11.25°	0	1	0	0	0	0
-22.5°	0	0	1	0	0	0
-45°	0	0	0	1	0	0
-90°	0	0	0	0	1	0
-180°	0	0	0	0	0	1
-354.375°	1	1	1	1	1	1

(a) PS logic pin mapping   (b) PS truth table
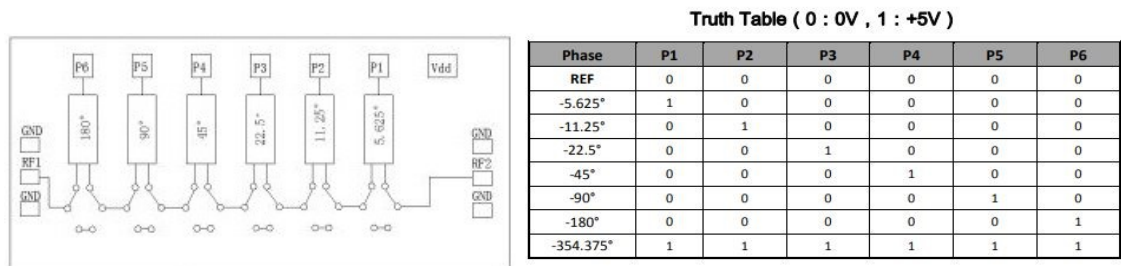
Figure 19: PS digital logic information [Confidential].

Figure 20 illustrates the MCU I/O signals that should be sent to the shift register for outputting a -50° phase shifted RF signal from a PS. It is assumed that shift register pin Q0 is connected to PS's P1 and P2 to Q3 respectively. $\overline{OE}$ is assumed to be low and $\overline{MR}$ high.
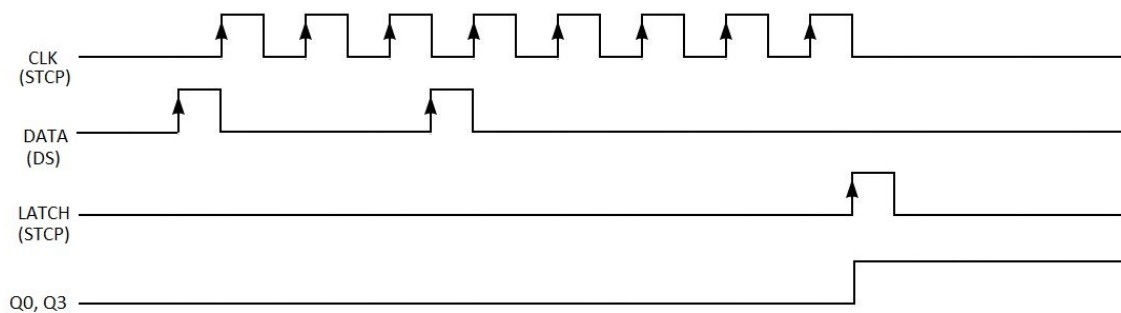
Figure 20: Shift register timing diagram example for setting a -50˚ phase offset for a PS.

3.3 RF Interface

The RF signal goes through the process as described in Section 3.1. Figure 21 illustrates the concept in the RF- domain.
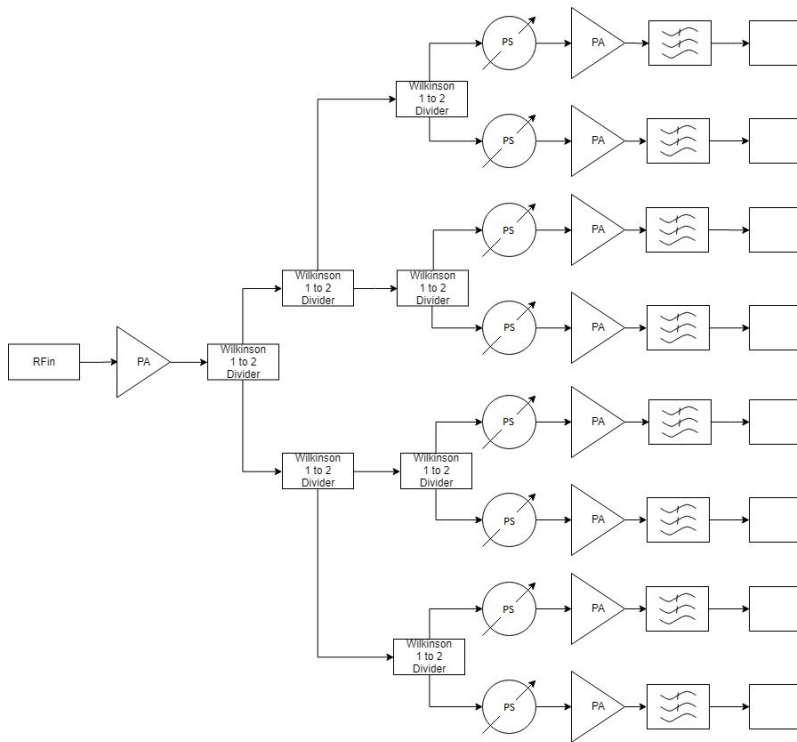
Figure 21: RF interface

System total attenuation had to be determined in order to choose the right amplifiers to achieve the specified system gain. A Wilkinson power divider halves the power after each branch [27, 28], thus the total attenuation provided by the power division circuit is approximately 9dB. The phase shifter has an average insertion loss of 5.5dB, and the maximum attenuation allowed for the LPF is 0.5dB.

A_{tot} is calculated in (12).

$$A_{tot} = A_{divider} + A_{PS} + A_{LPF} = 15dB \tag{12}$$

To achieve a gain that will be in the range of 3dBs to 5dBs for the system outputs, the PAs were chosen to have 10dB of amplification at the operation frequency bandwidth.

3.4 RF Microstrip Design

After estimating RF system requirements, the next step was to design and simulate the RF elements by using microstrips. The PCB parameters were set to εr = 4.6 and t was chosen to be 0.035mm. Simulations were performed with t = 0.05mm aswell. Height of the dielectric material h was set to 0.35mm in order to avoid abnormally wide traces for the RF transmission lines. PCB parameters are illustrated in Figure 22.
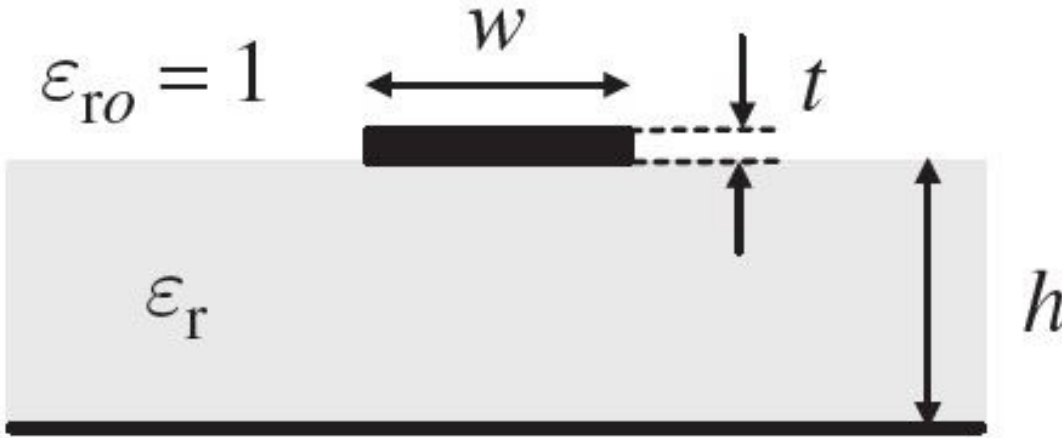
Figure 22: PCB parameter definitions, depicted according to reference [27].

Our system impedance was set to be 50Ω, since it is the characteristic impedance of the PAs and PSs. In order to determine the width of the transmission line to represent our system impedance, the ratio between w and h parameters is computed from (13) [28] and yields a value of 1.85.

$$\frac{w}{h} = \frac{2}{\pi}\left[B - 1 - \ln(2B - 1) + \frac{\varepsilon_r - 1}{2\varepsilon_r}\left(\ln(B - 1) + 0.39 - \frac{0.61}{\varepsilon_r}\right)\right] \qquad (13)$$

Where B is calculated by [28]:

$$B = \frac{60\pi^2}{Z_0\sqrt{\varepsilon_r}}$$
(14)

Which yields a value of 5.522. Since the ratio of the dimensions and H is known, the width of our 50Ω transmission line is computed to be 0.648mm.

3.4.1 Equal-split Wilkinson power divider

The Wilkinson Power Divider is used to divide RF power while achieving good isolation between ports and maintaining the desired impedance matching. The power division is based on quarter wave transforming, which is easily conducted by adding quarter wave lines on the PCB with specific impedances. The impedances connected to port 2 and port 3 will determine the widths of the power divider's quarter-wave transmission lines Z_{02} and Z_{03} [28, 29]. The Wilkinson power divider is illustrated in Figure 23.
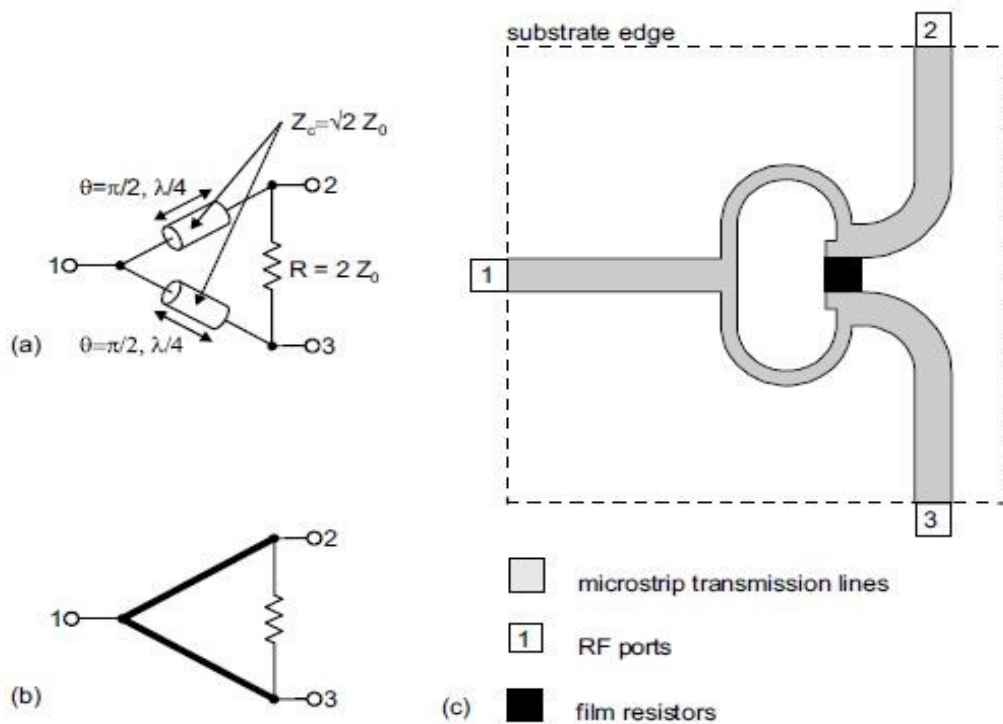
(a) Schematic, (b) electrical symbol and (c) layout of a microstrip realization

Figure 23: An equally split Wilkinson power divider, obtained from reference [29].

A constant *K* can be defined as [27]:

$$K = \frac{P_2}{P_1} \qquad (15)$$

Where P2 is the output power and P1 is the input power. Then the impedance of the quarter-wave transformers and the resistor can computed from the set of equations (16) [27]:

$$Z_{02} = Z_0 \sqrt{1 + \left(\frac{K}{1-K}\right)^2} \; ; Z_{03} = \frac{1-K}{K} Z_{02} \; ; \; R = 2Z_0 \qquad (16)$$

In our system, the desired power split was set to be equal, so *K* = 0.5, which yields Z_{02} = Z_{03} = 70.71Ω, and the value for the resistor depicted in figure 23 was computed to be 100Ω. By using equations (13) and (14), *w/h* yielded a value of 0.958 and $w_{70.71Ω}$ was computed to be 0.335mm. In order to determine λ_g, the $\mathcal{E}_{eff}$ is needed. First *F(w/h)* was obtained to be 0.272 from (17) [28]:

$$F(w/h) = (1 + 12h/w)^{-1/2} + 0.041(1 - w/h)^2 \qquad (17)$$

And $\mathcal{E}_{eff}$ to be 3.29 from (18) [28]:

$$\mathcal{E}_{eff} = \frac{\mathcal{E}_r + 1}{2} + \frac{\mathcal{E}_r - 1}{2} \; F(w/h) \qquad (18)$$

And the guided wavelength yields 45.95mm with (19) [28]:

$$\lambda_{g70.71Ω} = \frac{c}{f\sqrt{\mathcal{E}_{eff}}} \qquad (19)$$

The transmission line lengths of Z_{02} and Z_{03} was calculated with (20) [28] and yielded a value of 11.5mm

$$l_{70.71Ω} = \frac{\lambda_{g70.71Ω}}{4} \qquad (20)$$

If the matching conditions are satisfied at the design frequency defined by the quarter wavelength, the Wilkinson divider yields the following scattering matrix [27]:

$$[S] = \frac{-j}{\sqrt{2}}\begin{bmatrix} 0 & 1 & 1 \\ 1 & 0 & 0 \\ 1 & 0 & 0 \end{bmatrix}$$

(21)

In other words the reflection parameters (S_{11}, S_{22}, S_{33}) = 0 and isolation parameters (S_{23}, S_{32}) = 0. In an ideal situation, the divider would allow the transmission parameters to be exactly halved [27, 29]. However, in practice there are always some variations due to PCB manufacturing tolerances for example.

After microstrip parameter evaluation, simulations were performed for the power divider. Variables for microstrip dimensions were set according to previous calculations except for *w*. Figure 24 presents the simulation setup and the microstrip realization, the width of the 50Ω line was set to 0.315mm in this case.
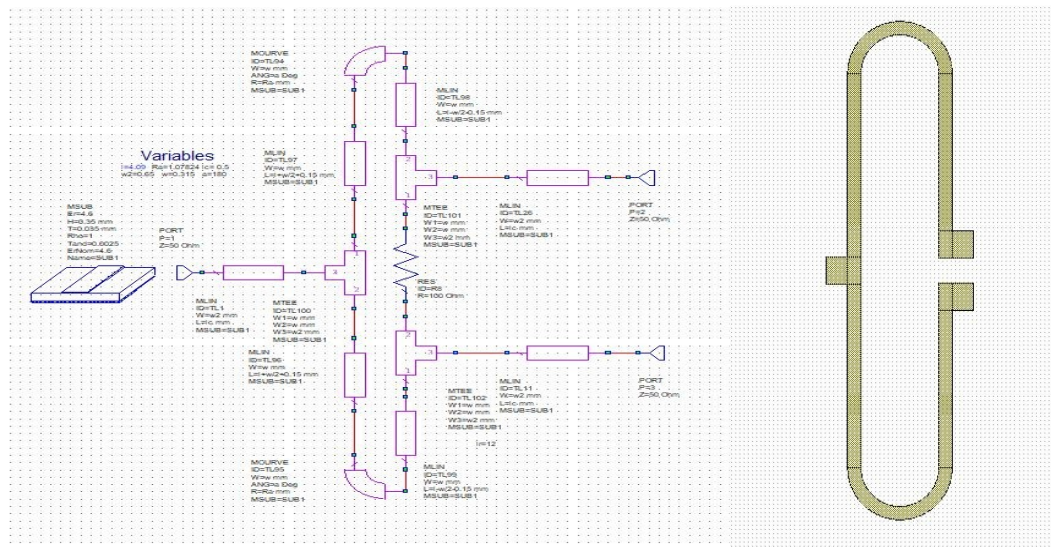
(a)Simulation setup for NI AWR   (b) Microstrip realization

Figure 24: Simulation setup and microstrip realization of the wilkinson divider.

Figure 25 presents the simulated response of the power divider.
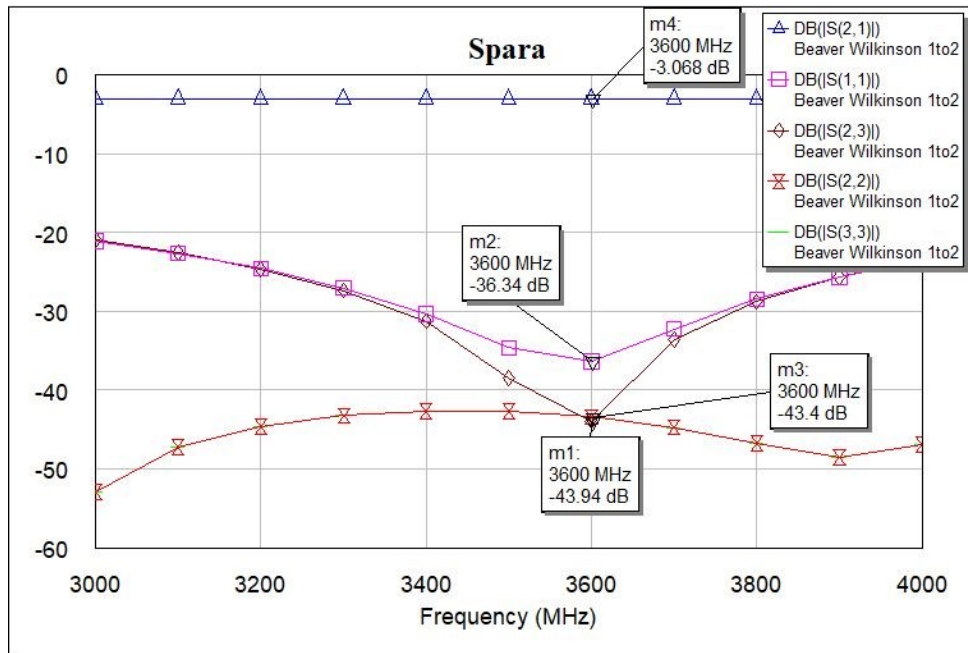
Figure 25: Simulation results of the Wilkinson divider.

Simulations implied great performance with the resonance frequency at the desired 3.6GHz frequency and the S_{21} behaving as predicted. The next step was to cascade the power divider to 8 outputs. Ideally this would yield us an attenuation of 9.03dB (22), where $n = 2\ldots 8$.

$$S_{n1[dB]} = 10log_{10}\left(\frac{1}{8}\right) \tag{22}$$

Figure 26 depicts the simulation setup and the response of the 8-way Wilkinson power divider.
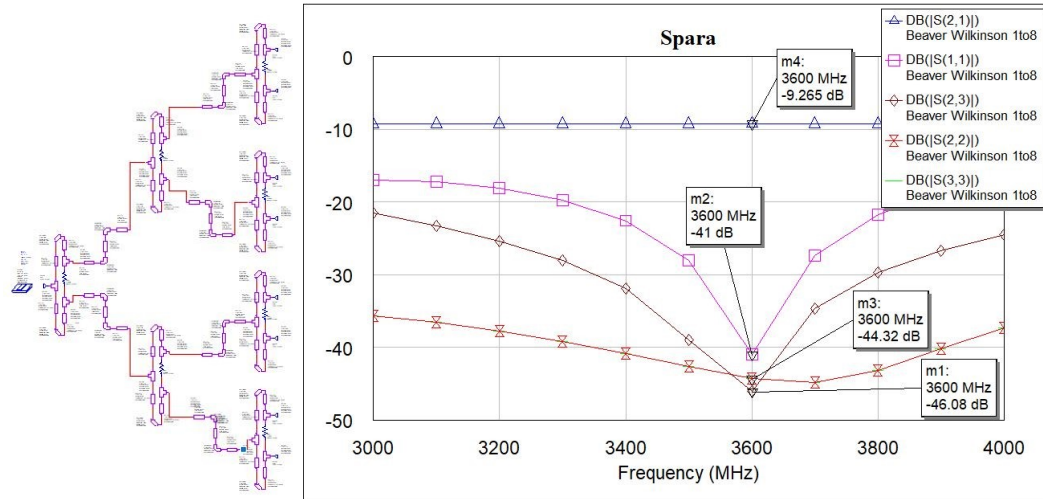
(a) 8-Way Wilkinson power divider setup (b) Simulated S-parameters

Figure 26: 8-way Wilkinson power divider realization and simulation.

A Monte Carlo analysis was also performed for the power divider in order to determine the approximate variance of the *S*-parameters. The tolerances were set according to Table 1.

Table 1: Tolerance values for the Monte Carlo Analysis.

Parameter	h	ε_r	w	t	R
Tolerance	±10%	4...4.6	±5%	±0.013mm	±5%

Results showed that S_{21} is not significantly affected by the tolerances. Reflection and isolation parameters stay below -16dB in the worst case scenario. Results implied that the design is sufficient.
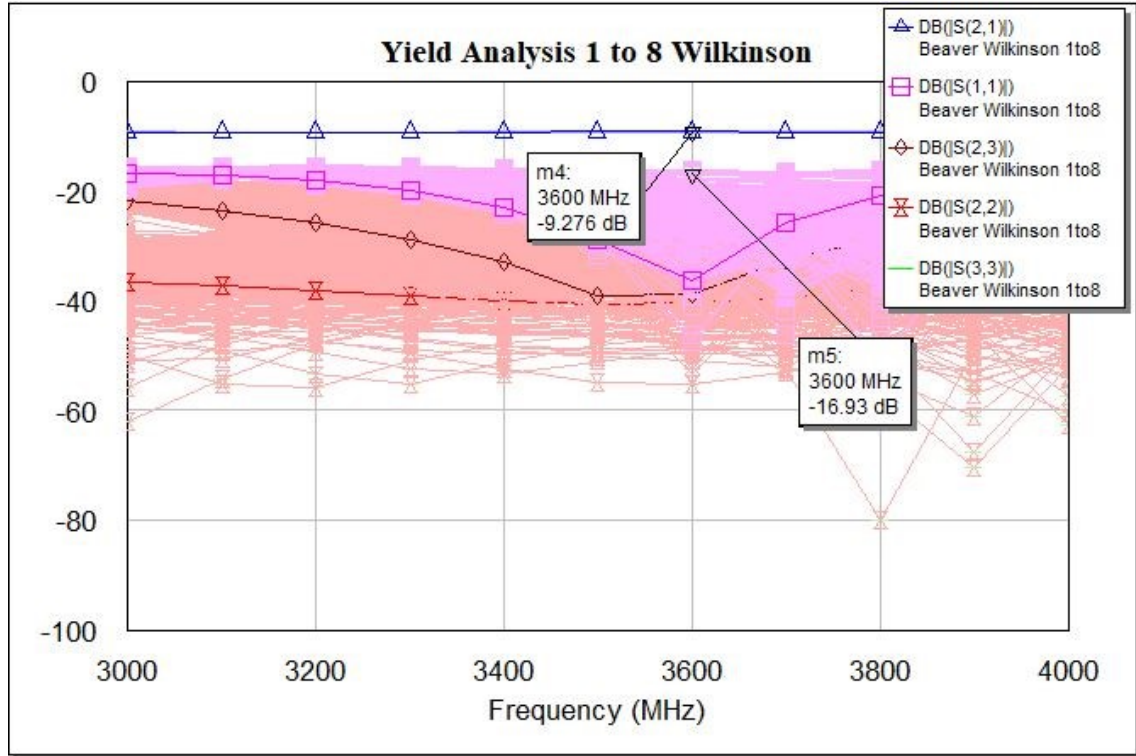
Figure 27: Yield a.k.a Monte Carlo analysis for the 8- way Wilkinson power divider.

3.4.2 SILPF with embedded OSCR

The low pass filter was designed to have a wide stopband and a steep cutoff. It is based on a Chebyshev response. The basic Chebyshev LPF response is obtained by (23) [29, 30]:

$$|H(j\omega)| = \left(1 + F_o C_n^2 \left(\frac{\omega}{\omega_c}\right)\right)^{-1/2} \tag{23}$$

Where C_n is a Chebyshev polynomial and L_r is the ripple factor in pass-band. L_r is defined by (24) [29]:

$$F_o = 10^{\frac{L_r}{10}} - 1 \tag{24}$$

Coefficients F_1, F_2, a_k and b_k for the filter are calculated from the set of equations (25).

$$F_1 = \frac{1}{4} \ln\left[\coth\left(\frac{L_r}{17.372}\right)\right] \; ; \; F_2 = \sinh\left(\frac{2F_1}{n}\right) \; ; \; a_k = 2\sin\left(\frac{(2k-1)\pi}{2n}\right) \; ; \; b_k = F_2^2 + \sin^2\left(\frac{k\pi}{n}\right)$$

(25)

Where $k = 1, 2, \ldots n$

From the equations above, the F_1 and F_2 values were computed to be 1.01473 and 0.41713 respectively. The a_k and b_k parameters for a 5th order chebyshev filter with 0.3dB passband attenuation are presented in the chart below:

Table 2: Calculated a_k and b_k parameters for the filter.

k	1	2	3	4	5
a_k	0.618	1.618	2	1.618	0.618
b_k	0.519	1.079	1.079	0.519	0.174

Then the g parameters for the filter are calculated the from equation set (26) [29] and the parameters are presented in Table 3.

$$g_0 = 1 \; ; \; g_1 = \frac{a_1}{F_2}; \; g_k = \frac{a_{k-1}\,a_k}{b_{k-1}g_{k-1}} \tag{26}$$

Where k = 2, 3 . . . n. Since n is odd in our case, $g_{n+1} = 1$ [29].

Table 3: Calculated gk parameters for the filter.

g_0	g_1	g_2	g_3	g_4	g_5	g_6
1	1.482	1.300	2.306	1.300	1.482	1

By using equation (27) [30] the value for cutoff was determined to be 1.0889, where ω was set to be 4.5GHz and ω_c = 4.9GHz.

$$\Omega c = \frac{\omega_c}{\omega} \tag{27}$$

The lumped element values were obtained with equation (28) [29, 30]:

$$L_i = \frac{Z_o}{g_0}\left(\frac{\Omega c}{\omega_c}\right)g_i \text{ , for i } = 1, 3, 5 \text{ and } C_i = \frac{g_0}{Z_0}\left(\frac{\Omega c}{\omega_c}\right)g_i \text{ for i } = 2, 4 \tag{28}$$

Element values for inductance and capacitance are presented in Table 4:

Table 4: Calculated values for capacitance and inductance.

i	L(nH)	C(pF)
1	2.62	-
2	-	0.920
3	4.077	-
4	-	0.920
5	2.62	-

The lumped elements can be transformed into equivalent microstrip lines by altering the impedances of the transmission lines by setting high impedance for the inductive lines and low impedance for the capacitive lines [33]. Figure 28 illustrates the modelling of the microstrip lines from the L-C ladder type of lowpass filters [33].
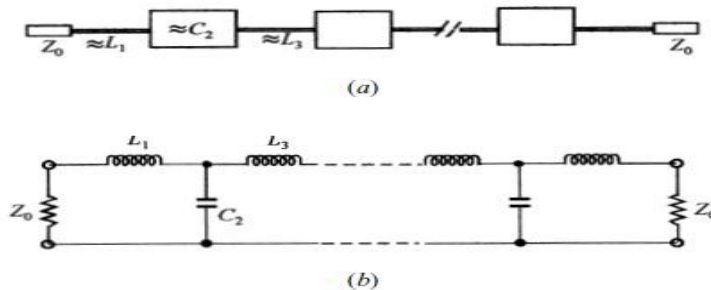
(a) General structure of the stepped-impedance lowpass microstrip filters. (b) L-C ladder type of lowpass filters [30].

Figure 28: Equivalent circuit of filter.

The inductive line was set to have a width of 0.2mm, which is a high impedance line. The width for the low impedance line which represents the capacitive line was set to be 3.2mm. The physical length for the high impedance (inductive) line was computed from equation (29) [31], for $I = 1, 3, 5$

$$L_i = \frac{60 l_{Li}}{v_0} \ln\left(\frac{8h}{w} + \frac{w}{4h}\right) \tag{29}$$

And the low impedance (capacitive) line by equation (30) [31], for i = 2, 4

$$C_i = \frac{\varepsilon_{eff} l_{Ci}\left[\frac{w}{h} + 1.393 + 0.667\ln\left(\frac{w}{h} + 1.444\right)\right]}{120\pi v_0} \tag{30}$$

The physical lengths of the transmission lines are presented in Table 5.

Table 5: Physical lengths of the low pass filter prototype.

i	l_{Li}(mm)	l_{Ci}(mm)
1	4.94	-
2	-	1.82
3	7.67	-
4	-	1.82
5	4.94	-

The microstrip realization of the prototype SILPF is presented in Figure 29:
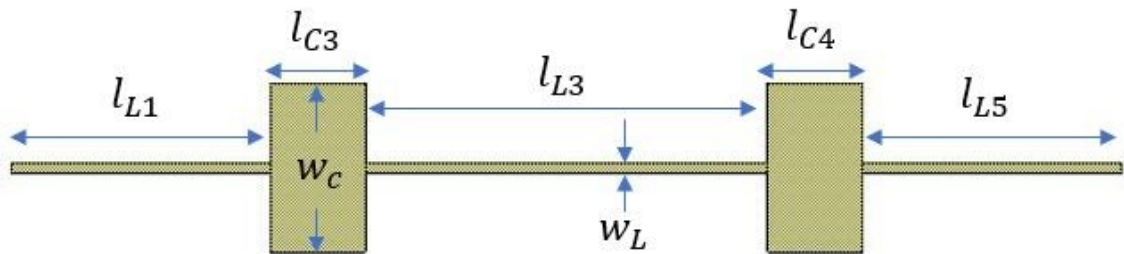
Figure 29: Dimensions of the prototype SILPF.

After the layout for the prototype was determined, simulations were performed. The simulation results of the SILPF prototype are presented in Figure 30.
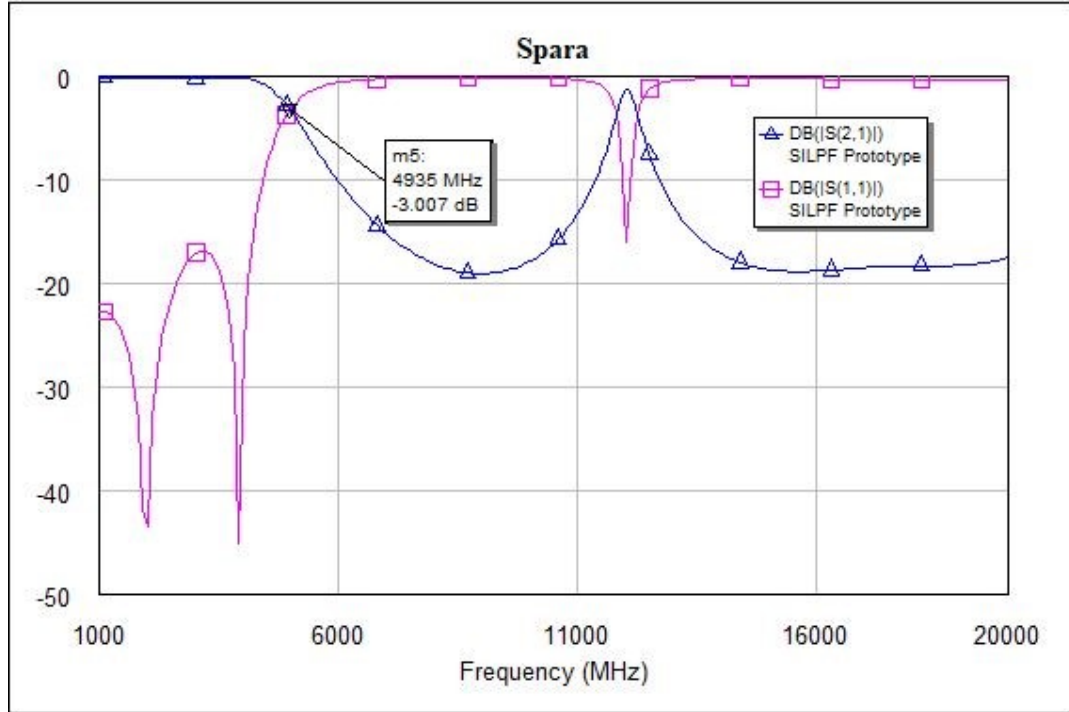
Figure 30: SILPF prototype S-parameter simulation.

Simulation results imply that the response of the filter is as expected.

Next step was to add an OSCR for the filter in order to achieve better stop band performance and to vastly sharpen the gradual roll-off [32]. The resonance frequency of the resonator is calculated with (31). Resonance frequency f_r was set to be 7.2GHz and L to 1nH. The equation yielded a value of 0.489pF for capacitance. The transformation from lumped element model to microstrip realization was computed with equations (29) and (30).

$$f_r = \frac{1}{2\pi\sqrt{LC}} \qquad (31)$$

Figure 31 illustrates the the equivalent circuits of the layouts.
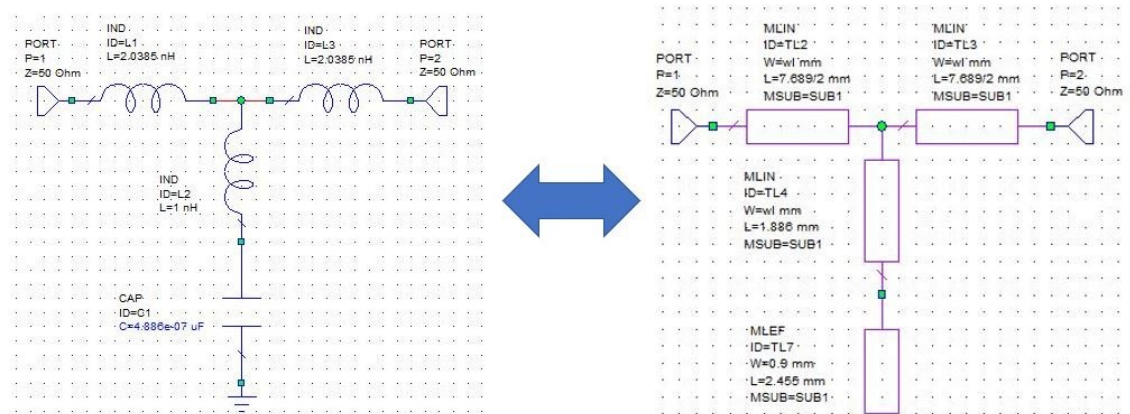
Figure 31: lumped and microstrip layouts of the resonator.

After the resonator was designed, it was added to the filter as depicted Figure 32:
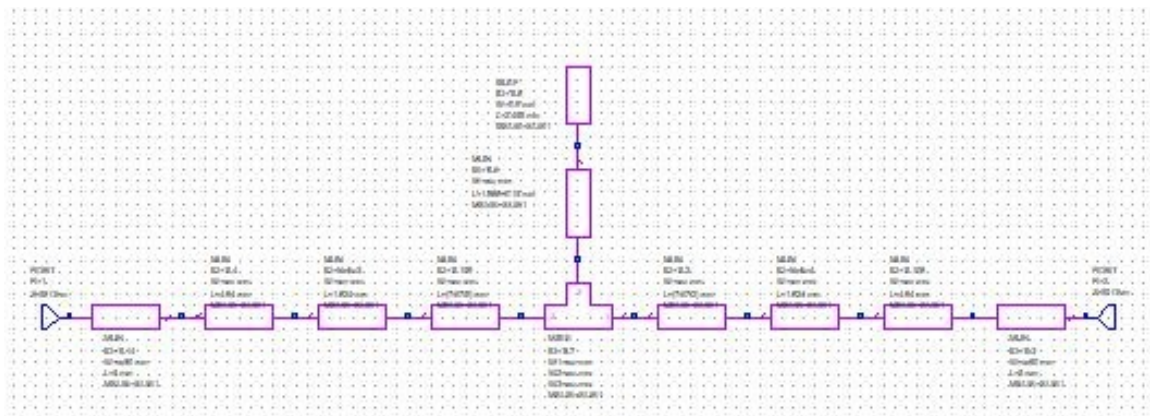
Figure 32: Layout of the SILPF with the embedded OCSR.

Implementation of the resonator to the filter yielded a better stopband performance with the cost of added passband ripple.
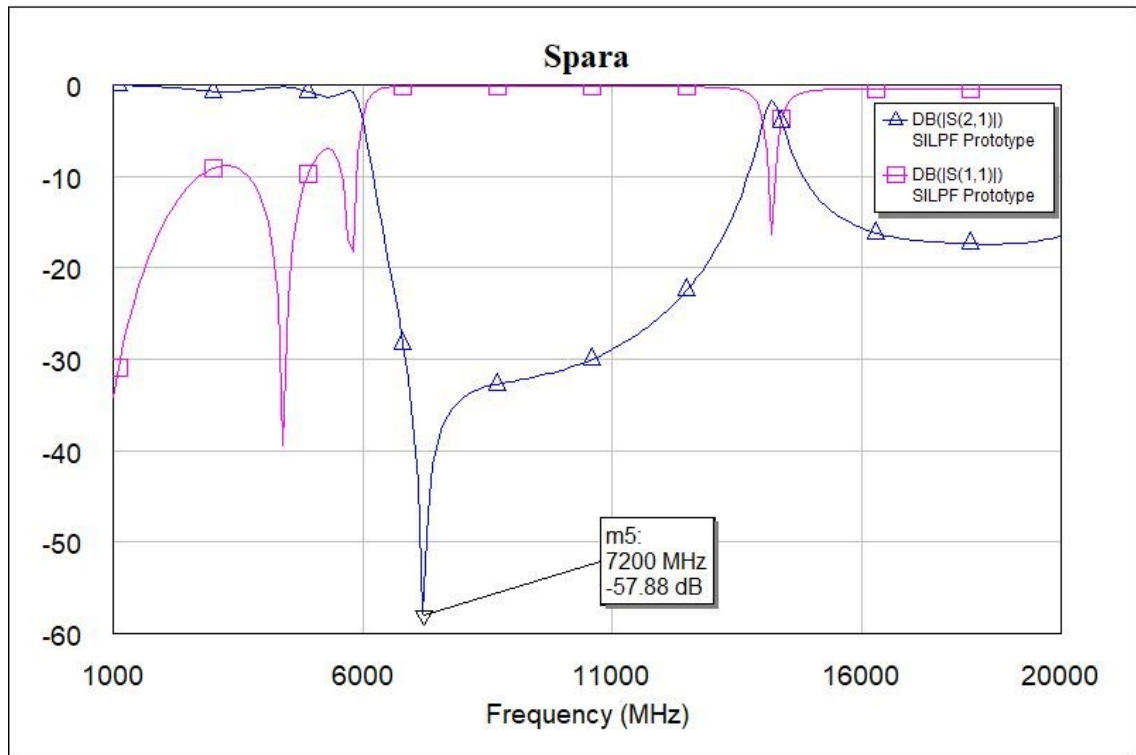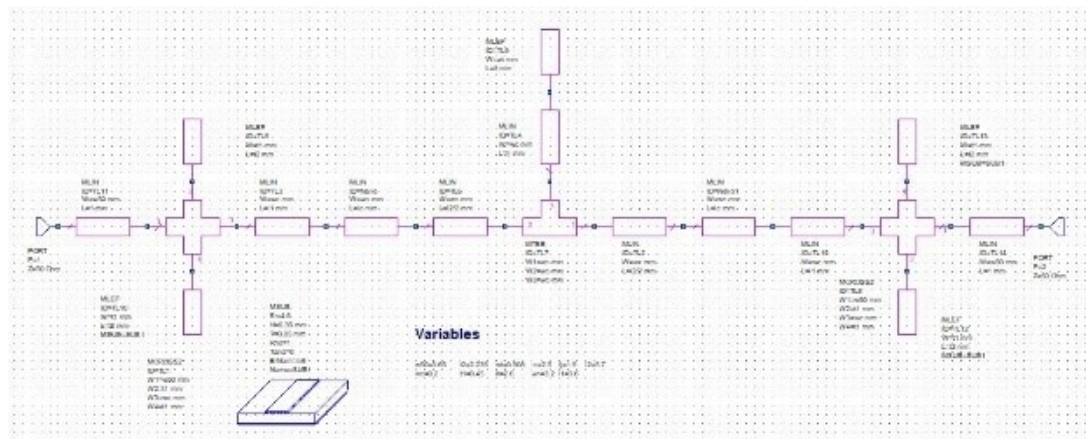
Figure 33 shows the simulation results of the filter.

Figure 33: Simulation of the SILPF with embedded OCSR.

To reduce passband ripple, improve S_{11} and group delay performance, impedance tuning lines were added to the filter [33] as depicted in Figures 34.

Figure 34: Final simulation layout of the SILPF with OSCR and impedance tuning lines.

The microstrip realization for the final filter design is depicted in Figure 35.
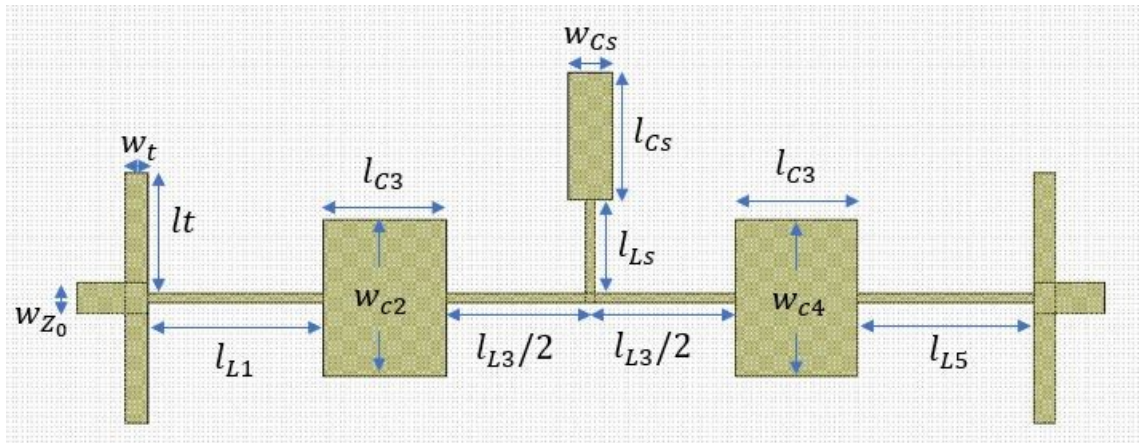
Figure 35: Final microstrip realization of the final filter.

The physical dimensions of the filter are presented in Table 6.

Table 6: Physical dimensions of the final filter.

i	l_L/w_L (mm)	l_C/w_L (mm)
1	3.6/0.2	
2	-	2.5/3.2
3	5.9/0.2	
4	-	2.5/3.2
5	3.6/0.2	

The dimensions of the OSCR and impedance tuning lines are presented in Table 7.

Table 7: Physical dimensions of the OSCR and rectangular patch combined feed lines.

Parameter (mm)	t	l_s	C_s
w	0.45	0.2	0.908
l	2.24	1.9	2.6

Simulation results after optimization are shown in Figure 36:
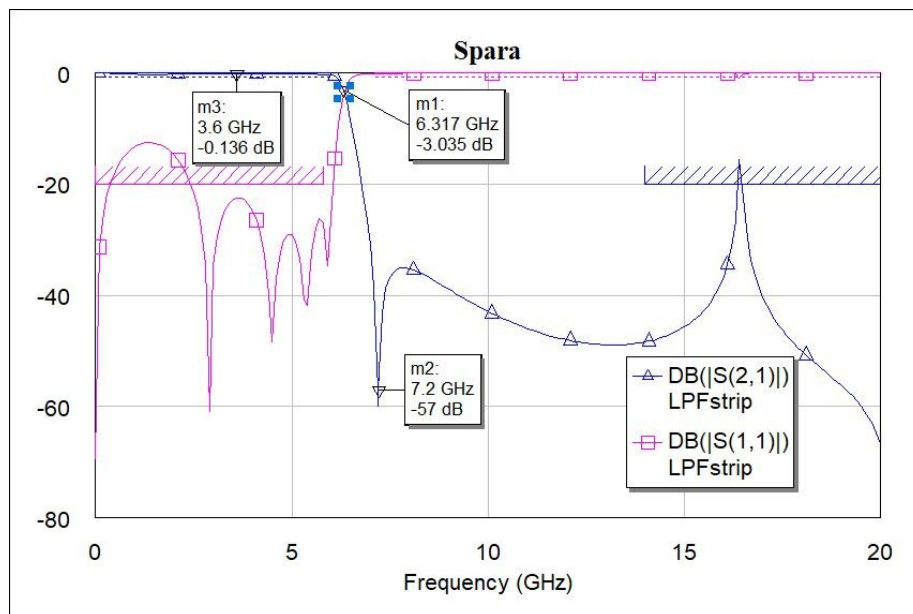
Figure 36: S-parameter simulation results after optimization of the final filter.

In order to maintain stable phase performance in the passband for the PSs, the group delay should have minimal amount of variance in the operating bandwidth. Figure 37 illustrates the simulated group delay performance and implies that performance is sufficient, since the operating frequency range is not near the ramp.
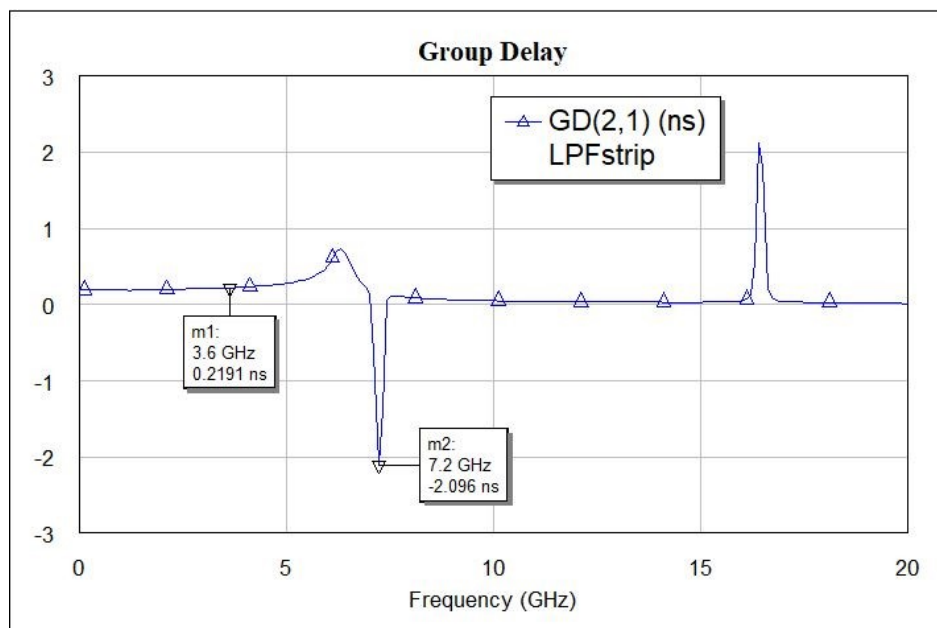

Figure 37: Group delay simulation results of the final filter.

Like for the Wilkinson power divider designed in Section 3.4.1, a Monte Carlo analysis was performed for the filter by using the same tolerance values according to Table 1. Figure 38 shows the Yield analysis performed for the final filter.
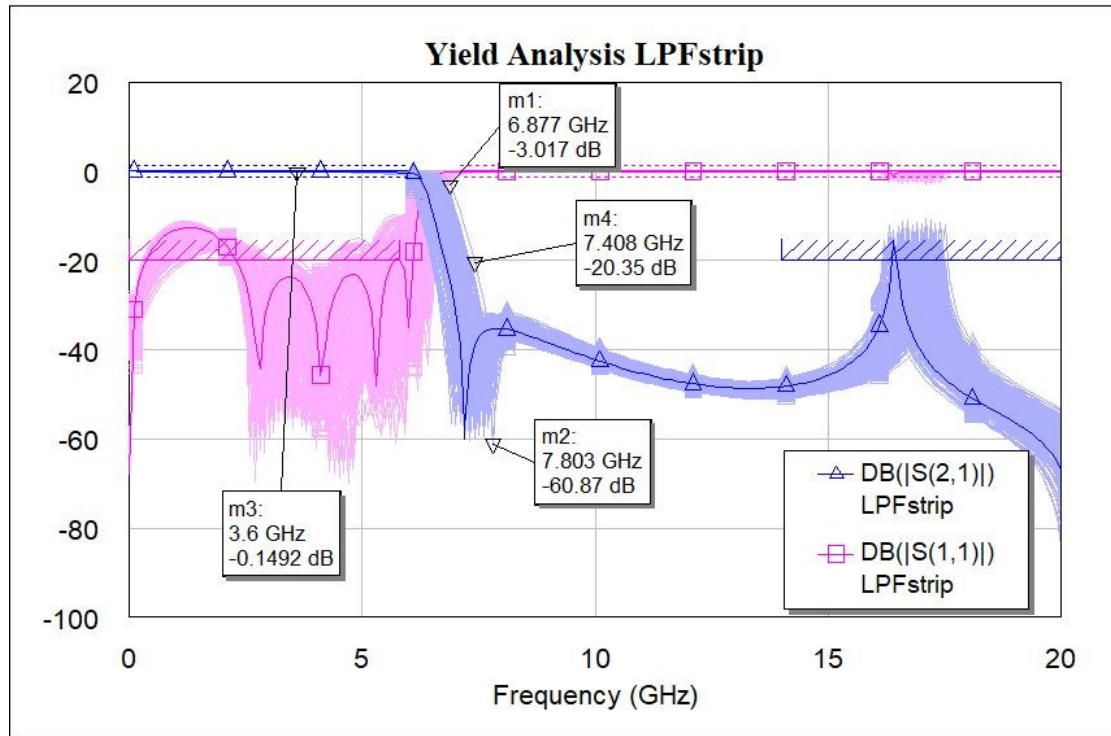

Figure 38: Yield a.k.a Monte Carlo analysis for the S-parameters of final filter design.

The analysis showed that that the passband and stopband were not severely affected. According to this simulation, at the worst case scenario the first harmonic of the 3.6GHz signal would be attenuated by about 20dB instead of 57dB and the notch would be transitioned to 7.8GHz. This implied that the filter satisfies the filtering requirements for the beamforming transmit system.

Yield analysis was also performed for the group delay simulation, which is shown in Figure 39.
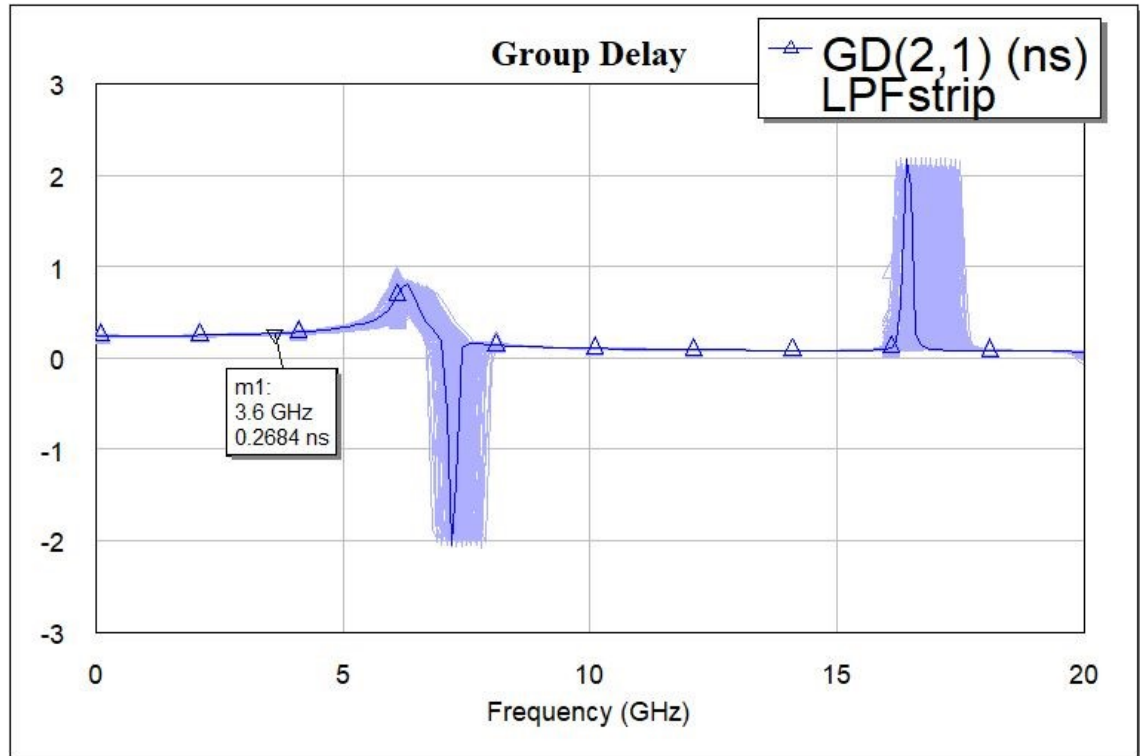

Figure 39: Yield a.k.a Monte Carlo analysis of the group delay of the final filter design.

Since the results indicated that the variance in the group delay was not severely affected in the operating bandwidth, it was determined that the filter's performance was sufficient enough for stable phase operation at the 5G midband (3.4GHz - 3.8GHz) frequencies.

3.5 Circuit schematics

Section contains the circuit design of the system. Previously designed and simulated RF components were imported to Mentor Graphics PADS software as DXF files. System operates on 5VDC.

3.5.1 RF input

Figure 40 shows the RF input circuitry. The component values surrounding the amplifier were obtained from the datasheet. Optional Pi-attenuators were placed before and after the amplifier in order to provide the possibility for gain adjustment during the testing process. The "SIGNAL_IN" off- page mark is connected to an SMA- connector. The positive operating voltage and connectors are shown in section 3.5.5. The outputs of the power divider were off-paged to the phase shifter chain and were named *PSn_RF_IN*, where *n* = 1...8. PS chain is shown in section 3.5.2.
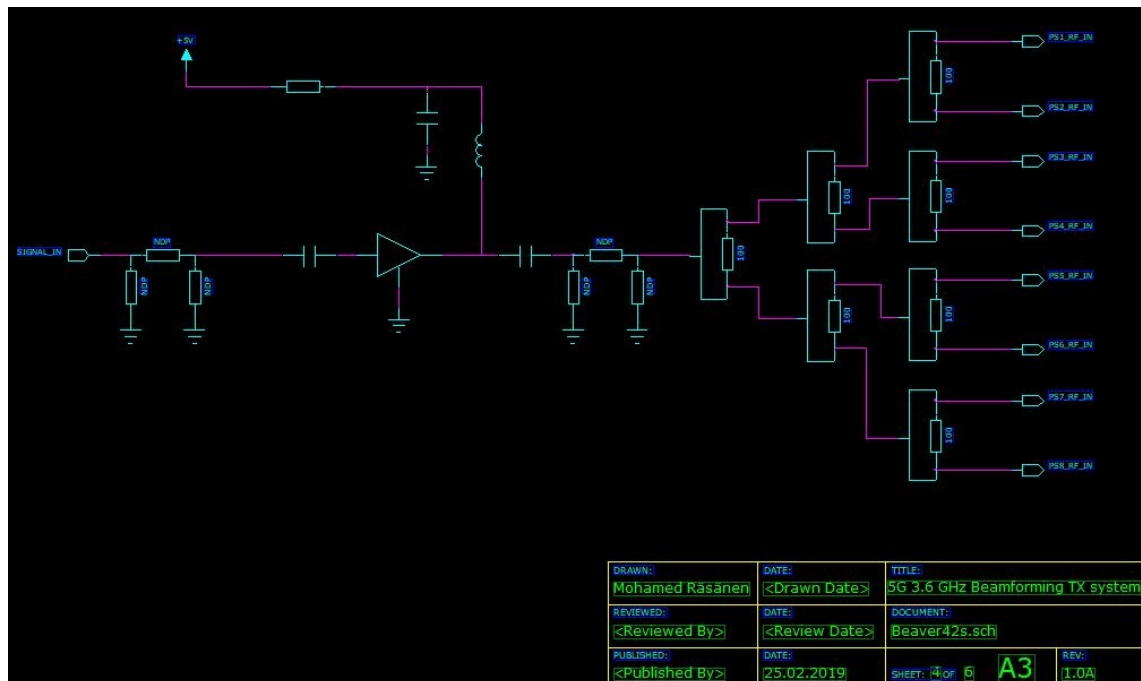

Figure 40: RF input circuitry.

3.5.2 Phase shifter chain

In Figure 41, the outputted RF-signals from the PSs are marked as *PSn_RF_OUT*, where n = 1…8, and are connected to the RF-output chain as shown in section 3.5.3. The digital control pins are depicted as *Pmn*, where *m* = 1…8 and resembles the regarded PS and *n* = 1…6 , which depicts the pin of the PS. The method for producing negative operating voltage for the PSs is shown in Section 3.5.5.
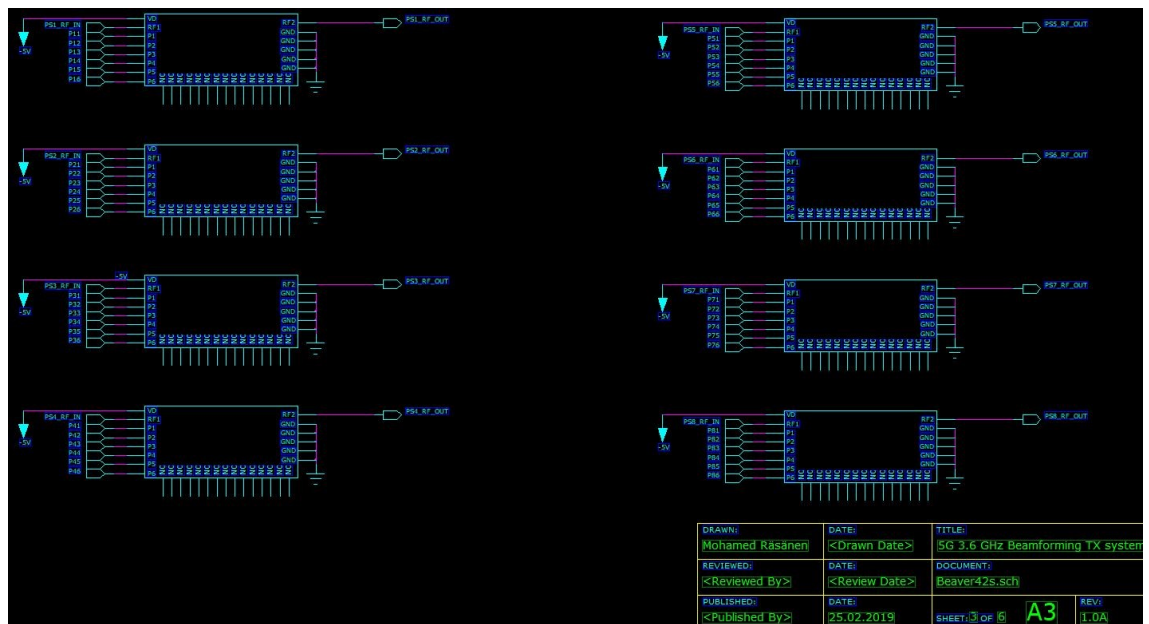

Figure 41: PS chain.

3.5.3 RF output chain

As Figure 42 implies, optional π- attenuators were added before the amplifiers for reasons described in section 3.5.1. Signal is filtered through the filter designed in section 3.4.2 and outputted to through the SMA connectors. Off-pages leading to the output SMA connectors are named *SIGNAL_n_OUT*, where *n* = 1...8 and are shown in section 3.5.5.
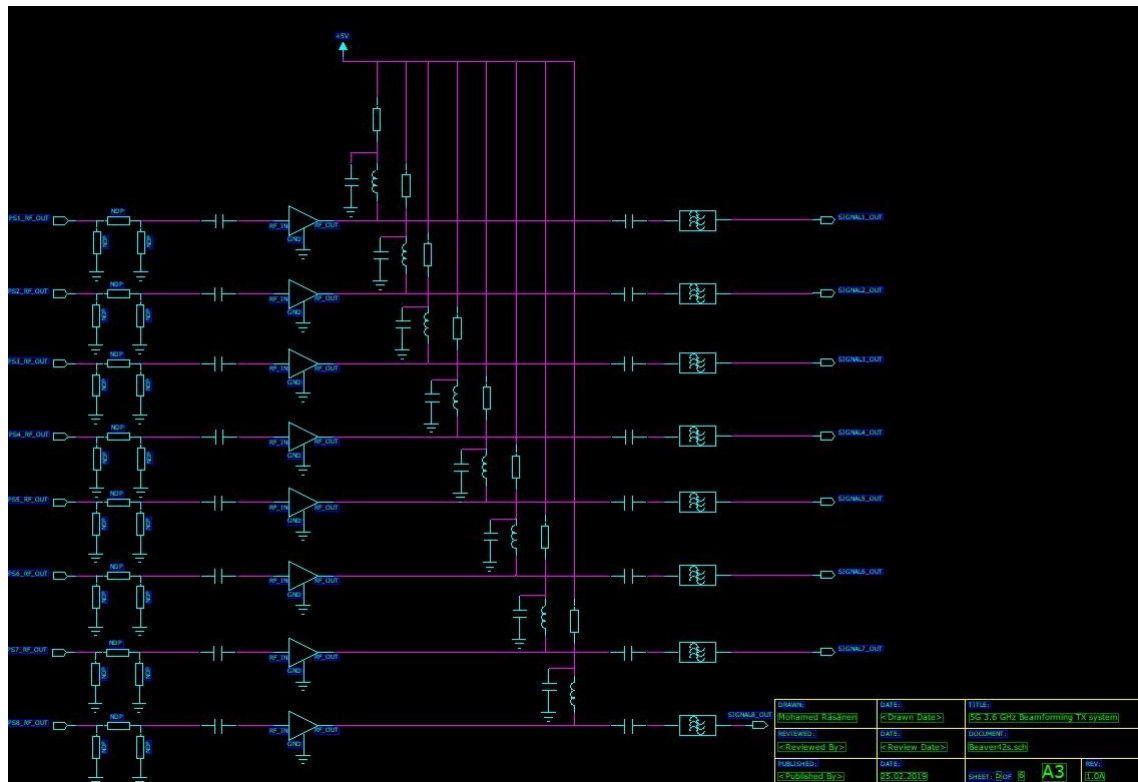

Figure 42: RF output circuitry.

3.5.4 Control logic chain

DS pin of the first shift register is connected to a connector which is for serial data input from the MCU. Serial data is then sent to the other shift registers from pins *Q7S* to *DS*. *STCP* and *SHCP* pins of the shift registers are connected to the remaining two I/O connectors assigned for the MCU. Logic output pins *Qn* are connected to PSs logic inputs, where $n = 1...8$. Parallel Indicator LEDs were added to logic output pins for visual feedback of the present logic state. The current limiting resistance for the LEDs is calculated from (32). The key thing is to ensure that the current consumption of the LEDs are not too high, otherwise there is not enough current for the logic to operate.

$$R = \frac{V_{in} - V_f}{I_f} \qquad (32)$$

Bulk and bypass capacitors were added between the Vin and GND pins. Control logic circuitry is depicted in Figure 43.
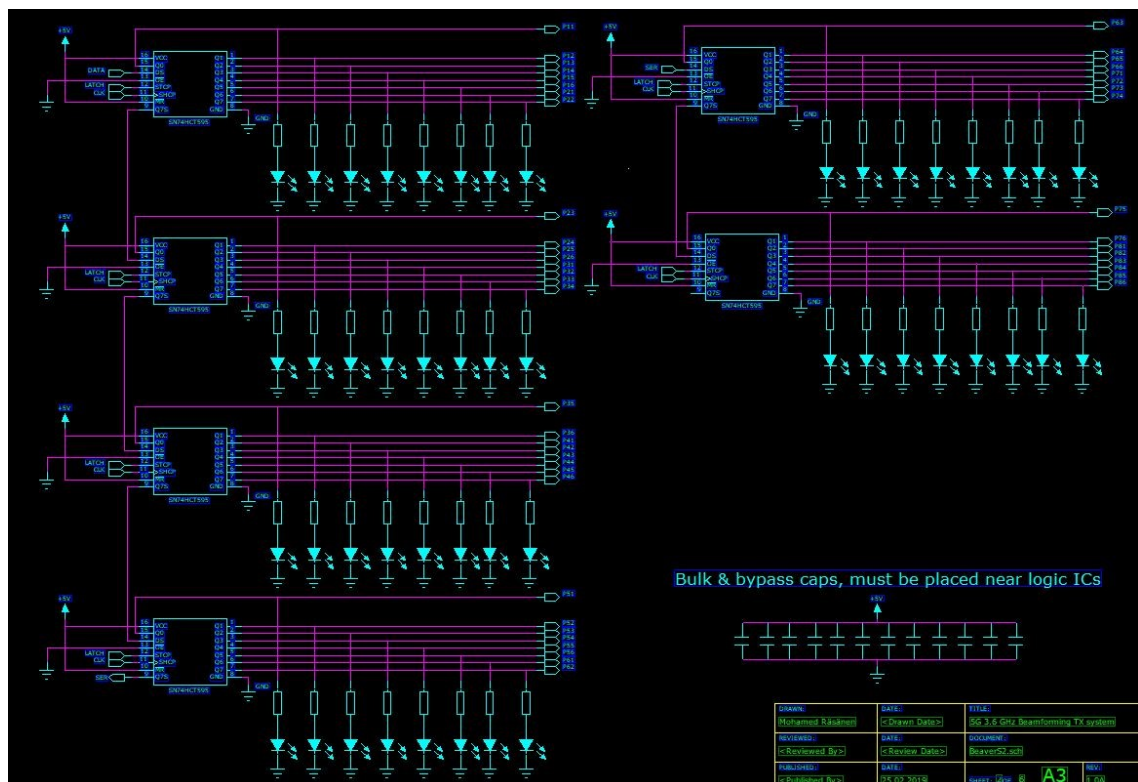

Figure 43: Control logic chain.

3.5.5 DC Power and connections

5VDC is fed through a reverse polarity protection circuit, which consists a PNP mosfet with low R_{DSon} acting as a switch. The voltage is inverted for the phase shifters with a DC voltage inverter. The resettable fuse selection was based on the total calculated current consumption of the components.

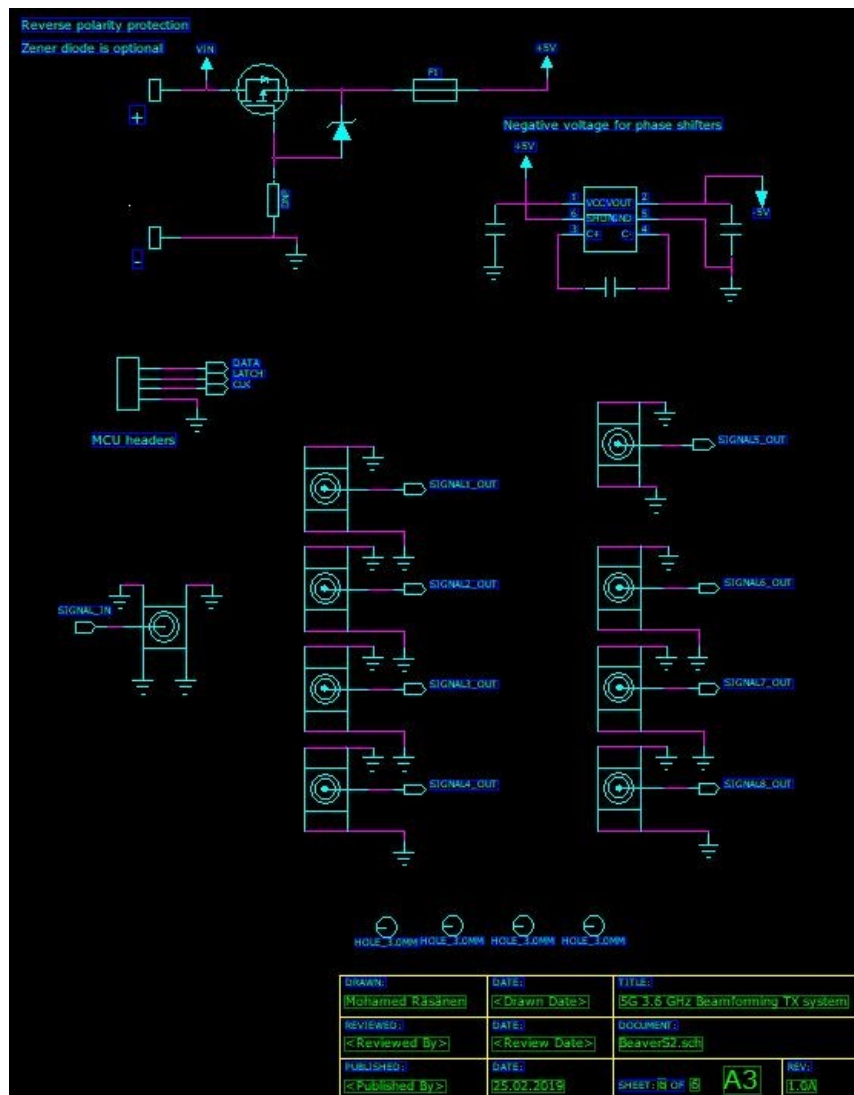Figure 44 shows the DC and connector circuitry.

Figure 44: DC power and connection circuitry.

3.6 PCB Design

This section contains the design process of the PCB. The circuit schematic from PADS Logic was transported to PADS Layout. First the layers were associated for the board. Components were then dispersed and placed with specific distances. The relative distances between the RF components were kept same in order to enable equal length tracing. After footprint layout the routing and ground plane flooring was performed. The relative differences between the lengths of the RF transmission lines were kept to a minimum in order to avoid large variances in phase offsets between the outputs. Figure 45 shows the top side of the PCB and illustrates the relative lengths.
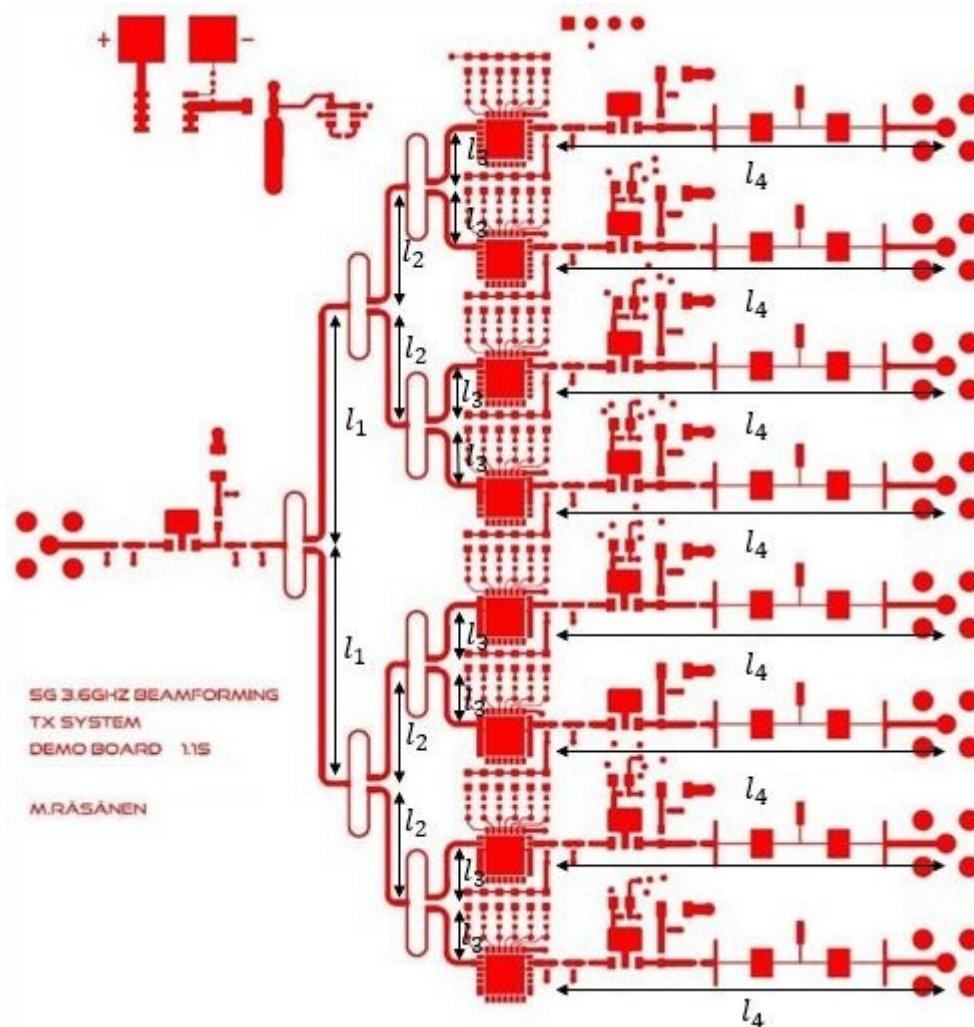

Figure 45: Top side of the PCB with relative RF transmission line length illustration.

3.7 System assembly and testing

The PCB was constructed by soldering and using a BGA rework station. It was noted during testing that the fuse selected was not suitable for this application and had to be switched, since it was stringetly limiting the current to the circuit. Additionally, there were some phase offsets between the outputs, thus calibration was performed through software by relatively zeroing the phase shifters with certain bit sequences. Variation between phase offsets was around $\pm 15°$ at the worst case. This was not due to PCB design, since after switching some of the PSs to new ones that were made by the same manufacturer, the offsets changed. After the PCB was ready, the mechanicanical casing was designed by a mechanical engineer in the company. The assembled PCB is shown in Figure 46, the shift registers are located on the other side of the PCB. The MCU was placed underneath the RF PCB.
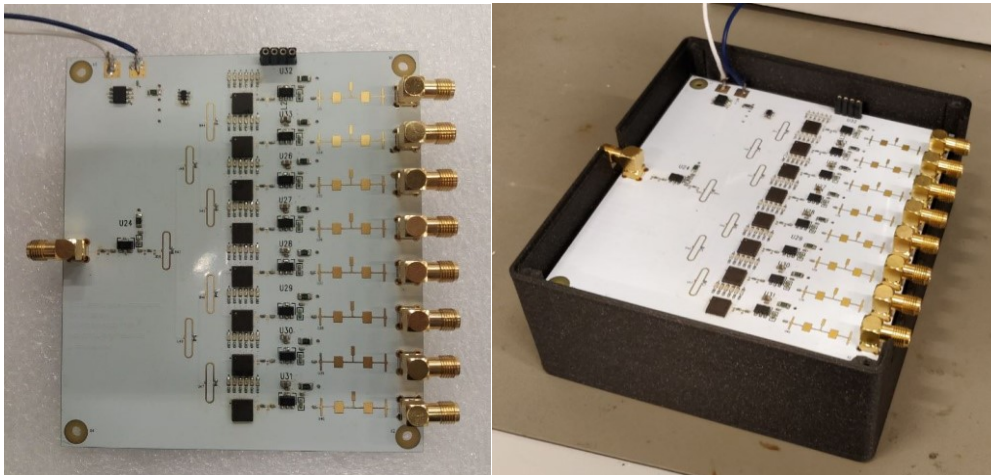
(a) Assembled PCB   (b) Assembled PCB with mechanics

Figure 46: Constructed analog beamforming transmit system.

Next task was to construct a phased array antenna and connect it to the RF PCB.

Figure 47 depicts the phased array antenna setup. The elements used were wideband pcb antennas.
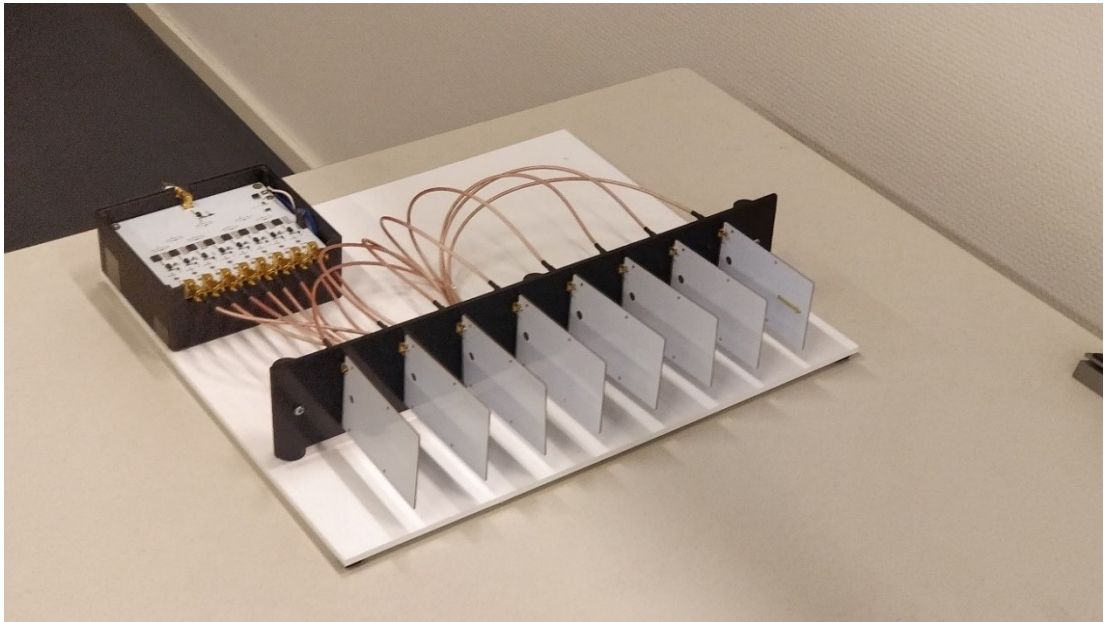

Figure 47: Linear antenna array with half-wave element spacing connected to the beamforming controller.

4 RF MEASUREMENTS

This section contains the radiation pattern measurements conducted with the designed beamformer. The transmit signal was set to be a sinusoidal signal at 0dBm power and the frequency was set to 3.6GHz. Antennas used in the array were wideband pcb antennas as mentioned in Section 3.7. The spacing between elements was 0.25λ. The measurement setup is shown in Figure 48.
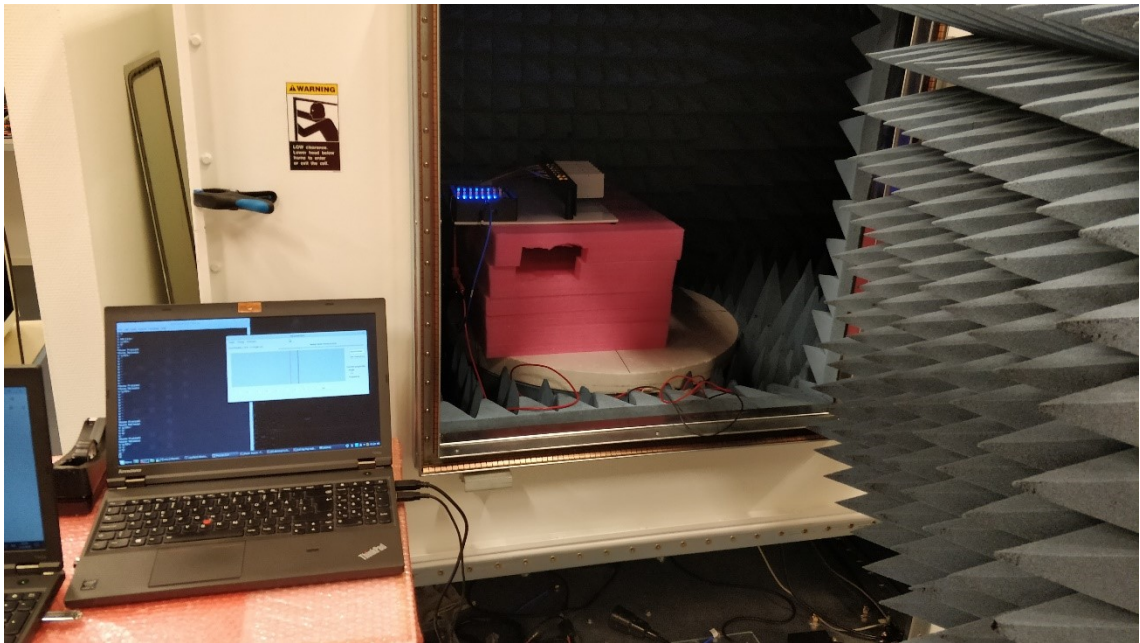

Figure 48: Measurement setup.

The measurements were performed in an anechoic chamber, in which the electromagnetic waves are absorbed by the RF absorbers. After the setup was deemed sufficient, the measurements were begun. Figures 48-52 show the measured radiation patterns for various steering angles with calibrated phase weightings. Results indicated that beamsteering was succesful. Sidelobes and main beam did not perform as expected before calibration and sometimes the setup was affected during the measurement process due to the placement of the cables. This led to an involuntary alteration of element and array positioning. A gain of about 18.5dB was observed accross all steering angles and the level of the nulls were dependent on the direction of the main beam.
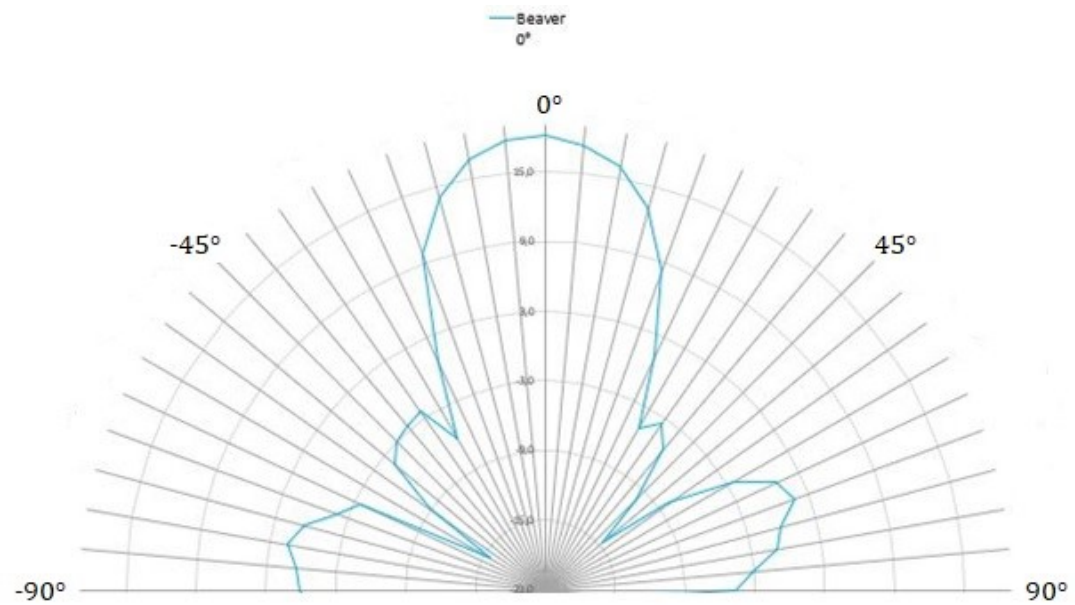
Figure 49: Transmit beamforming without beamsteering. Lowest null levels are at -15dB. One points at DOA of -60˚ and the other at +50˚.
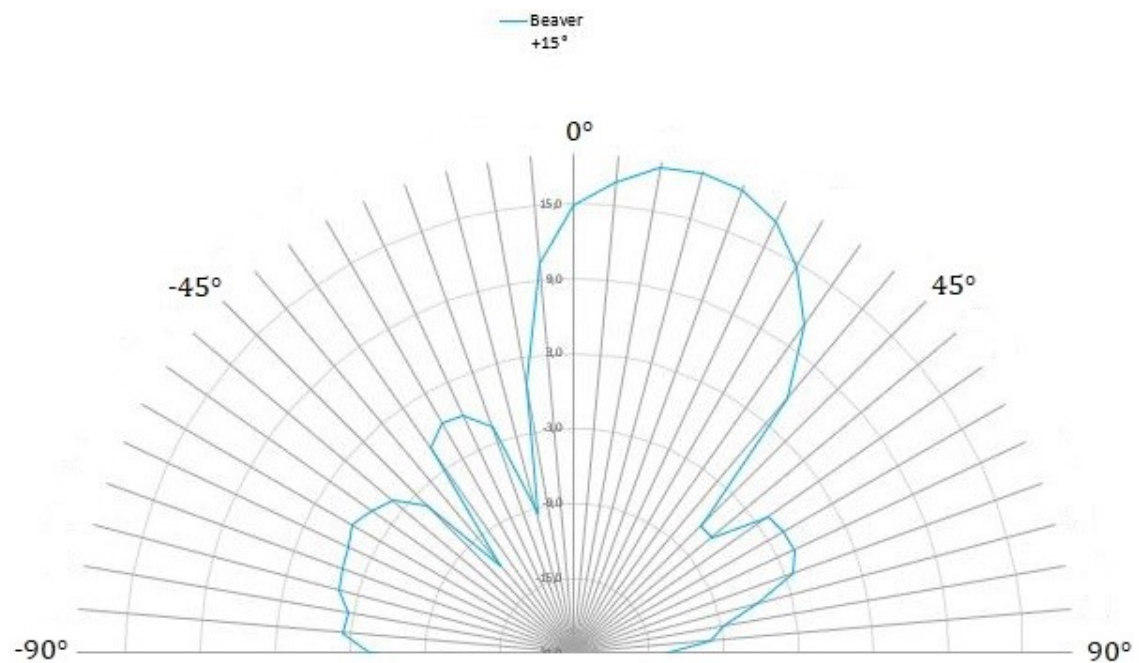

Figure 50: Transmit beamforming with a +15˚ phase shift. The lowest null points at DOA of -40˚.
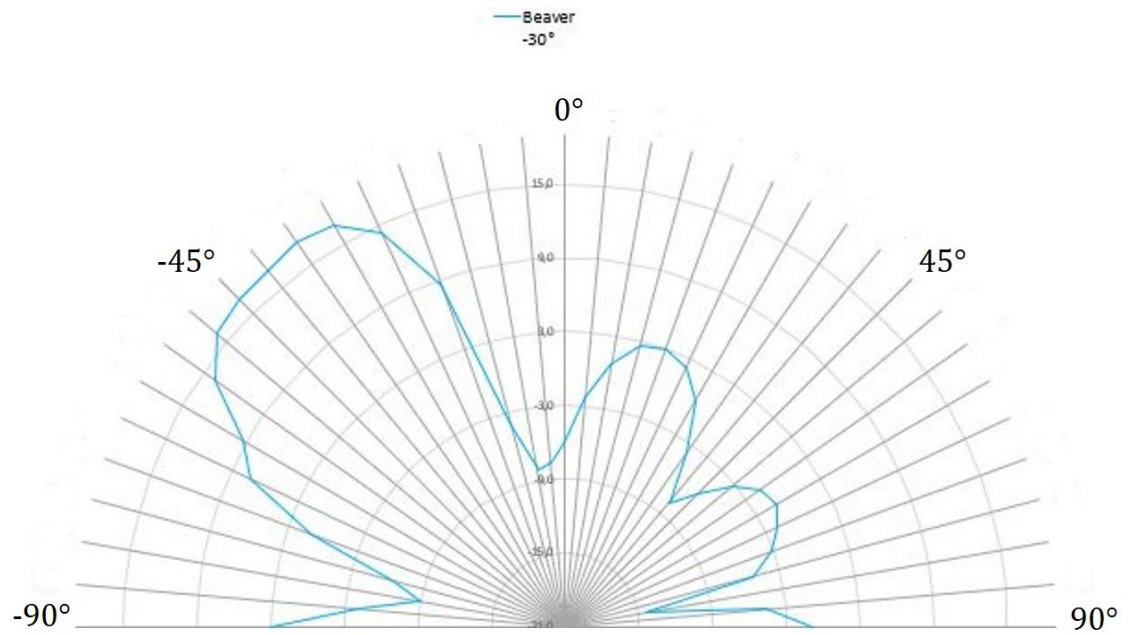
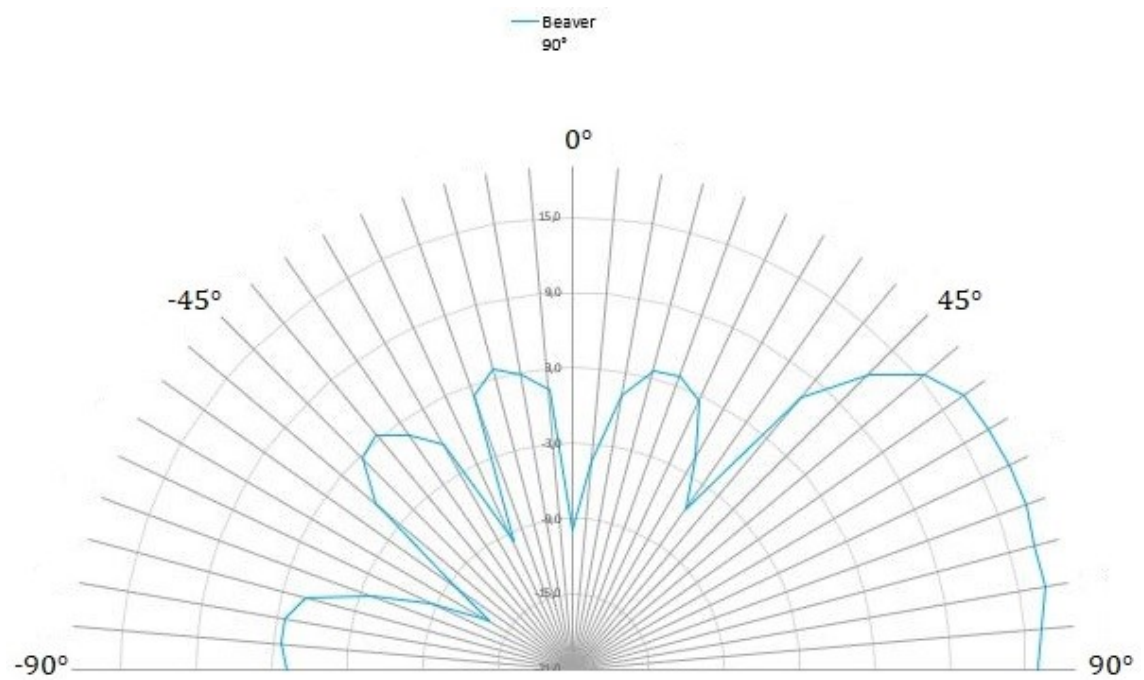Figure 51: Transmit beamforming with -30° phase shift. Increased number of sidelobes are now visible.

Figure 52: Transmit beamforming with 90° phase shift. The main lobe is now very wide and an increased number of sidelobes are now visible. Due to the quarter-wavelength spacing of the elements in the array, no grating lobes are observed in the visible region.

5 CONCLUSIONS

In this thesis different beamforming architectures were overviewed and an analog beamforming transmit system was designed for a 5G frequency band (3.4GHz – 3.8GHz) that is allocated for Europe. There were many procedures required to become started with the design, one of which was to obtain phase shifters that were not too costly compared to their performance. The low pass filter could have been implemented with a Bessel-type response due to its linear phase behaviour, however a wide stopband and a sharp cut-off were also requirements assigned for the system, which led to a modified Chebyshev design.

The beamformer yielded a gain of around 18.5 decibels across all steering angles and performed very well after sufficient calibration. Nulls and sidelobes were not always stable. The reason for this phenomenon could be the possible mutual coupling between the antennas, transmit power differences between the outputs, unaccounted variables in the measurement setup or some combination of these. Without the calibration, the radiationpatterns were not as distinguishable. The broadening of the mainbeam as a function of steering angle acted as predicted. The beamformer can be used for transmitting 5G midband frequency signals of 3.4GHz to 3.8GHz successfully.

Although the goal was reached in this thesis, there are many improvements that ought to be implemented. An advancement to the current system would be to replace the fixed power amplifiers to variable power amplifiers in order to provide amplitude control of the signals and thus, to obtain the ability to form increased number of radiation patterns. Additionally, signal reception circuitry could be designed to enable receive beamforming.

However, another solution could be to migrate towards on-off analog beamforming due to the ability of OABF to perform tasks required by MMIMO technology in the absence of phase shifters, as mentioned in Section 2.2.1. The reduction in cost is also something that should not be forgotten as hardware can easily become expensive.

REFERENCES

[1] Cisco: Global Mobile Networks Will Support More Than 12 Billion Mobile Devices and IoT Connections by 2022; Mobile Traffic Approaching The Zettabyte Milestone (2019). [Accessed: 30.05.2019].

URL: https://newsroom.cisco.com/press-release-content?type=webcontent&articleId=1967403

[2] Cisco Visual Networking Index: Global Mobile Data Traffic Forecast Update, 2017 – 2022 (2019). [Accessed: 30.05.2019].

URL: https://www.cisco.com/c/en/us/solutions/collateral/service-provider/visual-networking-index-vni/white-paper-c11-738429.pdf

[3] Q. Hu, M. Zhang, and R. Gao, "Key Technologies in Massive MIMO," *ITM Web Conf.*, vol. 17, p. 01017, 2018. ISSN: 2271-2097.

[4] C. I, C. Rowell, S. Han, Z. Xu, G. Li and Z. Pan, "Toward green and soft: a 5G perspective," in *IEEE Communications Magazine*, vol. 52, no. 2, pp. 66-73, February 2014. ISSN: 1558-1896.

[5] I. Villordo-Jimenez, I. E. Zaldivar-Huerta, and G. M. Galvan-Tejada, "An Overview of SDMA in Communications Systems," in *2006 49th IEEE International Midwest Symposium on Circuits and Systems*, San Juan, PR, 2006, pp. 168–171. ISSN: 1558-3899.

[6] A. Alexiou and M. Haardt, "Smart antenna technologies for future wireless systems: trends and challenges", IEEE Communications Magazine, Vol. 42, Issue 9, pp. 90-97, September 2004. ISSN: 1558-1896.

[7] E. Bjornson, L. Van der Perre, S. Buzzi and E. G. Larsson, "Massive MIMO in Sub-6 GHz and mmWave: Physical, Practical, and Use-Case Differences," in *IEEE Wireless Communications*, vol. 26, no. 2, pp. 100-108, April 2019. ISSN: 1558-068.

[8] T. L. Marzetta, "Noncooperative cellular wireless with unlimited numbers of base station antennas," IEEE Transactions on Wireless Communications, vol. 9, no. 11, pp. 3590-3600, Nov. 2010. ISSN: 1558-2248.

[9] Ahmed, Irfan & Khammari, Hedi & Shahid, Adnan & Musa, Ahmed & Kim, Kwang Soon & De Poorter, Eli & Moerman, Ingrid. (2018). A Survey on Hybrid Beamforming Techniques in 5G: Architecture and System Model Perspectives. IEEE Communications Surveys & Tutorials. PP. 1-1. 10.1109. ISSN: 1553-877X.

[10] 5G Spectrum GSMA Public Policy Position, November 2018. [Accessed 3.5.2019]

URL:https://www.gsma.com/latinamerica/wp-content/uploads/2019/03/5G-Spectrum-Positions.pdf

[11] L.Wei & W.Stephan: *Wide band beamforming: Concepts and Techniques,* , John Wiley & Sons, Incorporated, 2010, second ed, vol. 17. ISBN: 9780470661185.

[12] J.Okkonen (2013) *Unifrom linear adaptive antenna array beamforming implementation with a wireless open-access research platform,* Master's Thesis, University of Oulu, Depratment of computer science and engineering. [accessed 02.05.2019].

URL: http://warpproject.org/trac/wiki/PapersandPresentations

[13] M. Reil, G. Lloyd (10.2016) *Millimeter-Wave Beamforming: Antenna Array Design Choices & Characterization*, Rohde & Schwarz , White paper [Accessed 31.05.2019].

URL: https://www.rohde-schwarz.com/fi/applications/millimeter-wave-beamforming-antenna-array-design-choices-characterization-white-paper_230854-325249.html

[14] R.C. Hansen (2009) *Phased Array Antennas*, Wiley Series in Microwave and Optical Engineering Ser. Vol 213. ISBN: 978-0-470-40102-6.

[15] N.Fourikitis (2000) Advanced Array Systems, *Applications and RF Technologies*, Elsevier Science & Technology, first ed. ISBN 9780080498706.

[16] V. Venkateswaran and A.-J. van der Veen, "Analog beamforming in MIMO communications with phase shift networks and online channel estimation," *IEEE Trans. Signal Process.*, vol. 58, no. 8, pp. 4131–4143, Aug. 2010. ISSN: 1941-0476.

[17] S. Zhang, C. Guo, T. Wang, and W. Zhang, "ON–OFF Analog Beamforming for Massive MIMO," *IEEE Trans. Veh. Technol.*, vol. 67, no. 5, pp. 4113–4123, May 2018. ISSN: 1939-9359.

[18] S. Zhang, C. Guo, T. Wang and W. Zhang, "On-Off Analog Beamforming with Per-Antenna Power Constraint," *2017 IEEE 85th Vehicular Technology Conference (VTC Spring)*, Sydney, NSW, 2017, pp. 1-5. ISBN: 978-1-5090-5932-4

[19] Phased Array Antenna. URL: http://www.radartutorial.eu/06.antennas/Phased%20Array%20Antenna.en.html

[20] J.Litva, LO T.K.Y (1996) *Digital Beamforming in Wireless Communications*, Artech House, Norwood, MA, first ed. ISBN 9780890067123 p. 28-29

[21] P. Barton, "Digital beam forming for radar," in *IEE Proceedings F - Communications, Radar and Signal Processing*, vol. 127, no. 4, pp. 266-277, August 1980. ISSN: 0143-7070

[22] E. G. Larsson, O. Edfors, F. Tufvesson, and T. L. Marzetta, "Massive MIMO for next generation wireless systems," *IEEE Commun. Mag.*, vol. 52, no. 2, pp. 186–195, Feb. 2014. ISSN: 1558-1896.

[23] L. Lu, G. Y. Li, A. L. Swindlehurst, A. Ashikhmin, and R. Zhang, "An overview of massive MIMO: Benefits and challenges," *IEEE J. Sel. Topics Signal Process.*, vol. 8, no. 5, pp. 742–758, Oct. 2014. ISSN: 1941-0484.

[24] A. Alkhateeb, J. Mo, N. González-Prelcic, and Heath, Robert W. Jr., "MIMO Precoding and Combining Solutions for Millimeter-Wave Systems," IEEE, 2014. ISSN: 1558-1896.

[25] S. Han, C. L. I, Z. Xu, and C. Rowell, "Large-scale antenna systems with hybrid analog and digital beamforming for millimeter wave 5G," *IEEE Commun. Mag.*, vol. 53, no. 1, pp. 186–194, Jan. 2015. ISSN: 1558-1896.

[26] DIODES Inc. 74HCT595 Shift register datasheet. [Accessed 04.02.2019]

URL: https://www.mouser.fi/datasheet/2/115/74HCT595-259597.pdf

[27] F.Gustrau. *RF and Microwave Engineering : Fundamentals of Wireless Communications*, John Wiley & Sons, Incorporated, 2012. ISBN: 9781118349588

[28] I.Bahl (2003) *Lumped Elements for RF and Microwave Circuits*, Artech House, Norwood MA. ISBN: 9781580536615.

[29] R. Sorrentino. & B.Giovanni (2010) *Microwave and RF Engineering,* John Wiley & Sons Ltd, The Atrium, Southern Gate, Chichester, West Sussex, PO19 8SQ, Inc. ISBN: 9780470660218

[30] Jia-Shen G.Hong & M.J. Lancester (2011) *Microstrip Filters for RF/Microwave Applications,* Wiley Series in Microwave and Optical Engineering Ser, Hoboken, New Jersey, Vol.216, 2nd ed. ISBN: 9780470937280

[31] R.P. Clayton (2010) *Transmission Lines in Digital and Analog Electronic Systems*, John Wiley & Sons inc. 1st ed. ISBN: 9780470651407

[32] N.B.M. Hashim, M.S. Razalli, S.Z. Ibrahim and F. Farid, "Compact Ultra-Wideband Stepped-Impedance Low Pass Filter Utilizing Open Circuit Stub Resonator," *ARPN Journal of Engineering and Applied Sciences*, 2015. ISSN: 1819-6608.

[33] N. B. Binti Mohd Hashim, M. S. B. Razalli, S. Z. Binti Ibrahim, F. S. Binti Mahmu and N. Binti Mohamad Saaid, "Compact low pass filter with deep and wide stopband using H-shaped defected microstrip structure," *2016 3rd International Conference on Electronic Design (ICED)*, Phuket, 2016, pp. 558-562. ISBN: 978-1-5090-2160-4.